Product Validation and Intercomparison Report (PVIR) Phase 2

Version 1.0, 14 November 2025

Contents

Author	Approved	Signature	Date
Ben Timmermans, Guillaume Dodet	Fabrice Ardhuin, Annabelle OLLIVIER	A.Ollivier	19/11/2025
ESA Acceptance	Digitally signed by Sarah Connors Date: 2025.12.12 17:58:44 Z		

Issue	Date	Comments
1.0	November 2025	First version for ESA approval

List of Acronyms

ADP	Algorithm Development Plan
CCI	Climate Change Initiative
CDR	Climate Data Record
CDIP	Coastal Data Information Program
DD	Delay-Doppler
E3UB	End-to-End ECV Uncertainty Budget
ECMWF	European Centre for Medium-range Weather Forecasts
ECV	Essential Climate Variable
EW	Extra Wide-wath (for Sentinel-1 SAR)
IW	Interferometric Wide-swath (for Sentinel-1 SAR)
Hs	Significant Wave Height
L4	Level 4
LRM	Low Rate Measurement
MLE	Maximum Likelihood Estimator
NDBC	National Data Buoy Centre
PLRM	Pseudo Low Rate Measurement
PVIR	Product Validation and Intercomparison Report
PVP	Product Validation Plan
R.M.S.	Root mean square
RMSE	Root mean square error
RMSD	Root mean square deviation
SAR	Synthetic Aperture Radar
SI	Scatter Index
SSH	Sea Surface Height
S.D.	Standard Deviation
SWH	Significant Wave Height
TCA	Triple Collocation Analysis
USACE	U.S. Army Corps of Engineers
WP	Work Package
w.r.t	with respect to
WV	Wave Mode (for Sentinel-1 SAR)

1. Introduction

This document represents the Product Validation and Intercomparison Report (PVIR) for the Sea_State_cci phase 2 project, corresponding to Deliverable D4.1 of WP4000.

The purpose of the PVIR is to present results of consistency checks and validation of new CCI CDRs as described in the Product Validation Plan (PVP). The PVIR is a working document that is updated after each CCI product release, nominally following the initial production of a new version of the Sea_State_cci CDRs.

The PVIR is structured to address the requirements outlined in the ESA Statement of Work. In this report, validation results are presented into subsections as follows:

- Algorithm development (altimetry, S1 SAR) calibration / verification data summary [WP4110]: This section provides a summary of data verification activities undertaken during algorithm and CDR development ;
- Validation of Level-2 altimetry significant wave height [WP4130]: evaluation of L2p global significant wave height statistics from altimeters, and comparison with other reference data sources ;
- Validation of Level-4 gridded significant wave height [WP4120]: evaluation of consistency of global long term trends in significant wave height from the L4 gridded product, compared to other reference data sources ;
- Validation of sea state parameters from SAR imaging [WP4140]: evaluation of long term sea state parameters from Sentinel-1 SAR “Wave Mode” (global) and “Interferometric Wide” mode (global and coastal), and comparison with other reference data sources ;
- Conclusions and future work

Material in this document is being prepared for publication.

1.1 Scope of validation data and production timeline

Complete version 4 CDRs were finalised and released in September 2025. The scope of CDRs included within this release are shown in Table 1, which is an updated version of the original release scope and schedule captured in the PVP (Table 1). All of these datasets are included within the scope of this report, with the following exceptions due to resource and programme constraints.

Sentinel-1A/B EW mode developed by DLR, is explicitly excluded (highlighted in red), and only a preliminary validation of Sentinel-1A/B IW mode data (highlighted in amber) is provided (Section 5.4). These evaluations will be updated in future releases of this document. Note, however, that these datasets are substantial in both size and data diversity, comprising ~750,000 local fields of wave parameters (nearly 1 billion data points per parameter), mostly around coastal regions, and so an in-depth exploration of all aspects of this data is beyond the scope of this phase of the Sea_State_cci.

Note also that measures of uncertainty for sea state parameters are provided for all L2 products but these are excluded from evaluation in this report. This is in part due to resource constraints, and in part, to some extent these are accounted for through the data sampling required to produce the L4 gridded monthly CDR. Measures of uncertainty are expected to be included explicitly for monthly summary wave statistics in the version 5 L4 CDR.

Table 1: Planned production schedule for altimetry, SAR imaging and other sea state data and parameters

Altimetry datasets:

Version 4 (2024)	Version 5 (2026)
L2P - fix issues or shortcomings reported in v3, e.g.: ● SARAL retracking (improper definition of the boundaries of the sub-waveform to be fitted) ● some issues w/ancillary fields Retracking of selected altimeters: SARAL (to 2023), ERS-1, ERS-2 (complete), Jason-3 (to 2023), CryoSat-2 (to 2023); Included L2 from: Topex, S3A, S3B, S6 MF Revision of each processing step : averaging to 1Hz, editing, cross-calibration, uncertainties, ancillary fields, filtering, …. **L4** - Revision of content to 2023, based on all L2 data listed above.	fix issues or shortcomings reported in v4 adding new missions not covered in v1, v3, v4 and extending already included missions : HY-2B/C/D, GeoSat, SWOT, … revision of cross-calibration wrt to year 2 assessment Adding or enhancing the new variables tuned during Year 2 (uncertainty, other variables than Hs: sigma0/wind, …)

SAR datasets:

Version 4 (2025)	Version 5 (2026)
Sentinel-1 IW, EW and WV (DLR) Sentinel-1 WV (Ifremer)	ERS-1, ERS-2 WV (Ifremer, TBC)

1.2 Document structure

In the remainder of this document, we set out in more detail the activities, datasets and methods used throughout this document. Further sections of the document are structured as follows:

- Section 2 presents the sources of independent validation reference data to be used;
- Section 3 presents a summary of training / verification data, methods and references for algorithm development teams [WP4110]
- Section 4 describes validation of Level-2 altimetry significant wave height [WP4130]
- Section 5 describes validation of Level-4 significant wave height and uncertainty [WP4120]
- Section 6 describes validation of wave parameters from SAR imaging [WP4140]
- Section 7 summarises key findings from the CDR validation and future validation priorities.

2. Validation reference data general summary

In this section we summarise the reference datasets used to validate the version 4 CDRs. For both the altimetry (L2p and L4) and Sentinel-1 SAR wave mode CDRs, validation focuses on climatologies of significant wave height (Hs) and long term trends over global fields. For Sentinel-1 SAR interferometric wide mode, a more detailed, but limited, coastal scale evaluation is provided.

Prior to describing the reference datasets in Sections 2.2 to 2.6, we first summarise the sea state variables that have been produced, in Section 2.1.

2.1 Sea State Variables

A number of sea state parameters have been generated during Sea_State_cci version 4 CDRs. These are largely consistent with the format of earlier data versions released during Phase 1 of the project. For altimetry data, "denoised" Hs (Quilfen & Chapron, 2019; 2020) is provided, together with an uncertainty estimate per 1 Hz data point, and a range of supporting data including quality control flags and relevant match-up data from ERA5 reanalysis, provided for convenience (see also the Product User Guide). The DLR processing of Sentinel-1 WV mode and IW mode provides total Hs, windsea Hs, swell primary and secondary Hs, together with the first 3 moments of wave period (Tm0, Tm1, Tm2). The Ifremer processing of Sentinel-1 provides only total Hs. Note that only a subset of the DLR parameters, total Hs, Tm2 and swell primary Hs, are considered in this report. A list of parameters, partitions (where applicable), associated work packages and their anticipated version of release are shown in Table 2.

Table 2: Sea state parameters for validation.

Parameter	*Formal definition (from dir. integrated surface elevation power spectral density E(f))*	*Algo. Dev. WP Team (Missions)*	*CDR version*
n^{th} moment (used in the definition of other parameters)	$m_n=\int E(f)\, f^n\, df$ Note that the moment is extended beyond the high frequency limit of model or data, usually using a f^{-5} tail.		
Total sig. wave height Hs	$Hs = 4\sqrt{m_0}$	WP2410 Nadir altimetry (L2/L3/L4) WP2440 (All)	4
Mean Period $T_{m0,2}$ (T_{m2}, T_Z)	$T_{m0,2}=(m_0/m_2)^{1/2}$	WP2440 DLR (S1-A/B) ODL (S1-A/B)	 4 5
Partition parameters	Windsea SWH (DLR) Partition 1 & 2 SWH (DLR)	WP2420 DLR (S1-A/B) Ifremer (S1-A/B)	 4 5

2.2 In Situ Data

2.2.1 Description

The use of in situ data, typically from moored buoys, in this version of the PVIR is limited to algorithm team internal calibration and verification activities, where it has been used extensively. This is summarised in Section 3.

2.3 Wave Model Data

While wave model data are not the result of a wave measurement, they provide continuous long term global data coverage for a range of sea state parameters a valuable source of intercomparison, and a means of generating a large number of collocations with satellite data. Models can also provide full spectral output and additional parameters related to wave energy sources and sinks (such as whitecap information).

However, deficiencies associated with errors in forcing field (winds, currents, sea ice) errors or lack of representation of some physical processes (swell dissipation, wind-wave generation, wave breaking …) and errors caused by limitations in numerical schemes lead to very important errors in wave model spectral shapes. Energy levels for some frequencies and directions can be off by more than one order of magnitude (e.g. Alday & Ardhuin, 2023), and biases that vary in space and time. Long period swells are the most prone to errors as they are very sensitive to forcing and parameterizations in very small regions at the centre of storms, and suffer the most from imperfect numerical schemes that do not represent the continuous frequencies and group speeds of real waves, but instead use discrete frequencies and directions.

Intercomparison with model data is well motivated since models tend to be quite accurate for many applications, and are both convenient and widely used. However, (dis)agreement between observations and models does not confer (lack of) accuracy on either dataset.

In this report, two datasets derived from numerical models are used for intercomparison.

2.3.1 Non-assimilating models

Resource Code long term high-resolution European wave hindcast

Version 4 of the Sea_State_cci CDRs includes previously unseen data arising form the DLR processing of Sentinel-1 interferometric wide-swath mode. This data is well suited to nearshore and coastal applications, with a particular abundance of data over European seas. It comprises successive spatial fields taken along-track, with an image coverage of approximately 250 km x 250 km, with a spatial resolution of approximately 5 km per grid cell (see e.g. Figure 6.14). Furthermore, up to 8 sea state parameters (wave heights, periods, etc) are provided per 5 km cell, which motivates the need for more abundant data sources for intercomparison and validation, particularly close to the coast.

At such spatial scales, in situ data is almost universally unavailable, so in this PVIR we exploit the “ResourceCODE” long term wave hindcast (Accensi et al. 2019). The following text is reproduced from the publication, but note that since the initial release of the hindcast, it has been updated to 2024. Wave parameters, and in many locations, complete directional spectra, are provided hourly on a spatial resolution at sub-kilometre scale near the coast.

"The ResourceCODE tool suite is supported by a comprehensive hindcast database of high-resolution ocean energy resource parameters for European waters. The configuration of the ResourceCODE wave hindcast model is based on a high-resolution unstructured grid extending from the south of Spain to the Faroe Islands and from the western Irish continental shelf to the Baltic Sea. Forcing winds are extracted from the ERA5 database while the currents and water levels are recomposed from a database of harmonics of tidal currents (MARS and FES2014). These forcing fields have been used to run WAVEWATCH-III® to generate a 28-year metocean database covering the [1993-2020] period with an hourly time step. A set of 39 global parameters as well as the frequency spectra are made available as output at each of the 328 000 nodes of the grid while directional spectra are provided on a coarser grid. The model configuration and dataset have been extensively validated against measurement data, both in situ and remote. Special consideration was given to the assessment of the spectral distribution of the energy within sea-states spectra."

Details of the comparisons between the DLR Sentinel-1 IW mode data and the ResourceCode hincast are provided in Section 6.4.

2.3.2 Assimilating models

ERA5 monthly reanalysis

The European Centre for Medium Range Weather Forecasts (ECMWF) reanalysis dataset, ERA5 (Hersbach et al. 2020), is ubiquitous in geophysical sciences. It also represents one of the most widely used sources for wind and wave data (Aarnes et al. 2015; Timmermans et al. 2020a). Note, for example, that the ResourceCode hindcast (Section 2.3.1) is forced using ERA5 wind fields. As such, it is important that Sea_State_cci CDRs are intercompared with ERA5 sea state data. We note, however, that in spite of its wide use, several studies, including those associated with Sea_State_cci Phase 1, have raised questions over the stability of the long term wave climate record in ERA5, likely linked to step changes in assimilation schemes and source data (Meucci et al. 2020; Timmermans et al. 2020). ERA5 assimilates a variety of remotely sensed data, including wave height data from altimeters. Historically this includes Jason-2 and SARAL Altika, but is currently limited to Cryosat-2 (ECMWF, personal communication). A number of other altimeters (Jason-3, Sentinel-3A/B and Sentinel-6A) are assimilated operationally, but not included in the ERA5 reanalysis. Efforts are underway to improve the historic and ongoing stability of the sea state record in the forthcoming ERA6.

In this report, ERA5 monthly fields are used to intercompare climatological values of sea state parameters in various ways. Typically the native ERA5 wave fields, which are provided on a grid at 0.5° x 0.5°, have been linearly interpolated using standard tools to a 2° x 2° grid. Note that monthly fields are limited to providing only mean values of sea state parameters, and that, although hourly data is available and may be used to derive more detailed information, such as higher percentiles and extremes, it is not used in this version of the report.

Details of the comparisons between ERA5 monthly significant wave height fields and both altimeter and SAR data are provided in Sections 4 and 6.2 respectively. Comparisons between the sea state parameters of DLR Sentinel-1 WV mode data are provided in Section 6.3. Long term trends for monthly Hs from ERA5 are shown in Section 5.2.

2.4 Other Satellite Measurements

Owing to the wide inclusion of historic and current satellite missions and sensors into Sea_State_cci CDRs, independent reference data from satellites is somewhat limited. Furthermore, the lack of detailed examination and reprocessing as applied through the Sea_State_cci leaves many questions about the reliability of those mission data excluded from the project.

The most notable and relevant alternative source of sea state observations from satellite altimeters, calibrated into a consistent product, is the long term Level-2 global dataset of Ribal & Young (2019). This dataset has been consistently updated to provide recent data under a consistent calibration approach, hereafter referred to as RY2023. Noting that these datasets are widely used, it is important that Sea_State_cci CDRs are intercompared to identify areas of (dis)agreement. RY2023 is described further in Section 2.4.1.

2.4.1 Ribal & Young [RY2023] intercalibrated altimeter record

The dataset of Ribal & Young (2019) is widely used and incorporates nearly all available historic sea state observations from low resolution (LR) mode (and pseudo-LRM for SAR mode altimeters) nadir-pointing altimeters. It spans the complete altimetry record dating back to Geosat, launched in 1986, and is updated on an approximately annual cycle to incorporate the most recent observations. Data from different missions are intercalibrated using a methodology based upon in situ data, somewhat similar to Sea_State_cci. Since this dataset is based on the same original altimetry observations, a strong statistical consistency between RY2023 and Sea_State_cci CDRs is unsurprising. Nonetheless it was shown by Timmermans et al. (2020), and noted in the PVIR version 3, that global climatological summary statistics, and long term trends in Hs, differed appreciably between the two datasets. This has highlighted the possible impacts of mission intercalibration methodology on the long term sea state record (Young & Ribal, 2022).

In this report, RY2023 data are typically intercompared with Sea_State_cci data by producing global climatological fields through aggregating 1 Hz observations on a 2^o x 2^o grid.

We note also that the RY2023 dataset differs somewhat from Sea_State_cci in terms of sea state and environmental parameters provided. For example, RY2023 provides estimates of both sigma0 (C + Ku bands) and wind speed components, together with an estimate of wave period, based on an empirical algorithm from altimetry data. These additional variables are not considered in this version of the PVIR.

2.5 Known Challenges For Data Intercomparison

With the growing diversity of sea state parameters beyond significant wave height, notably those produced from SAR processing, such as wave periods, partition parameters and directional information, the probability of discrepancy between data sources may increase. For example, this may affect sea state parameters with sensitivity to the calculation of the spectral tail. While significant wave height is likely to be somewhat insensitive to this issue, during

Sea_Phase_cci phase 1, it was identified that processing methods for wave period, likely linked to machine learning training data gave rise to somewhat artificial discrepancy in wave period Tm2. This was detailed in version 3 of the PVIR (see Section 2.5.1 below).

More generally, as the diversity of satellite sensors and processing methods grows, in particular anticipated in the forthcoming version 5 of the Sea_Phase_cci CDRs, and elsewhere, we caution users to be aware of such evolving discrepancies.

2.5.1 Sensitivity of wave period evaluation to spectral frequency cut-off

In situ observations such as those made by buoys are limited in their ability to observe high frequency waves above a cut-off frequency f_C ~ 0.4 - 0.5 Hz. However, wave models generally discretize their spectrum in the range, 0.035Hz < f < 0.5 - 1.0 Hz, but generally the frequency range is extended to infinity, by assuming a f^{-5} high frequency tail, such as done in WAM and Wavewatch III. Historically, models have output T_E, but T_{m02} (T_Z) and T_1 are also common. T_{m02} is often available from in situ observations, but not necessarily the wave spectrum. Therefore, if one is unable to recompute the mean periods, does the choice of f_C matter when comparing mean wave periods between observations and model output?

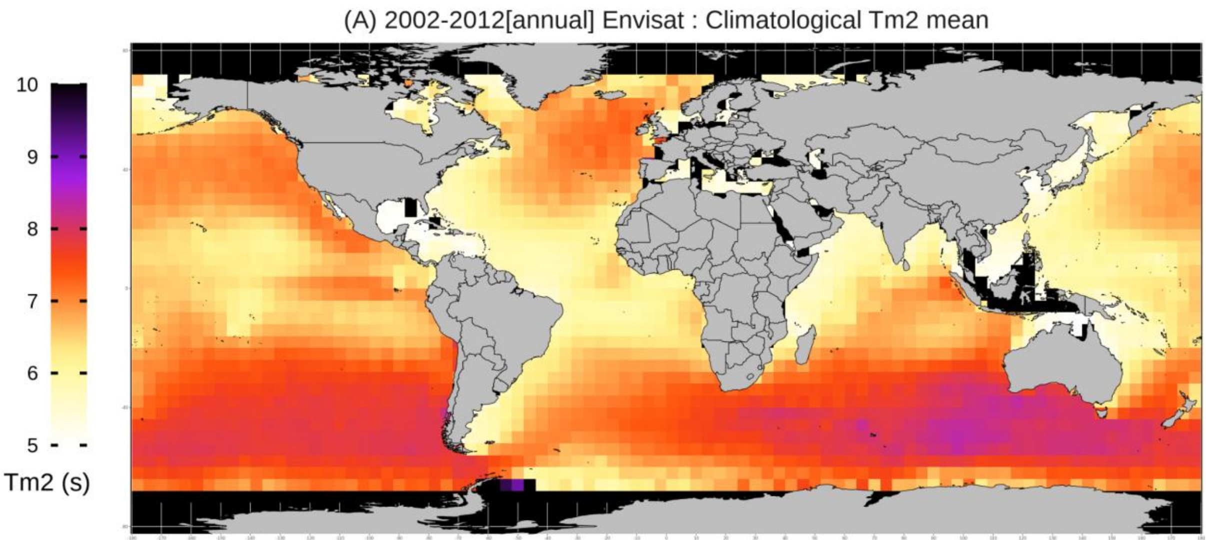

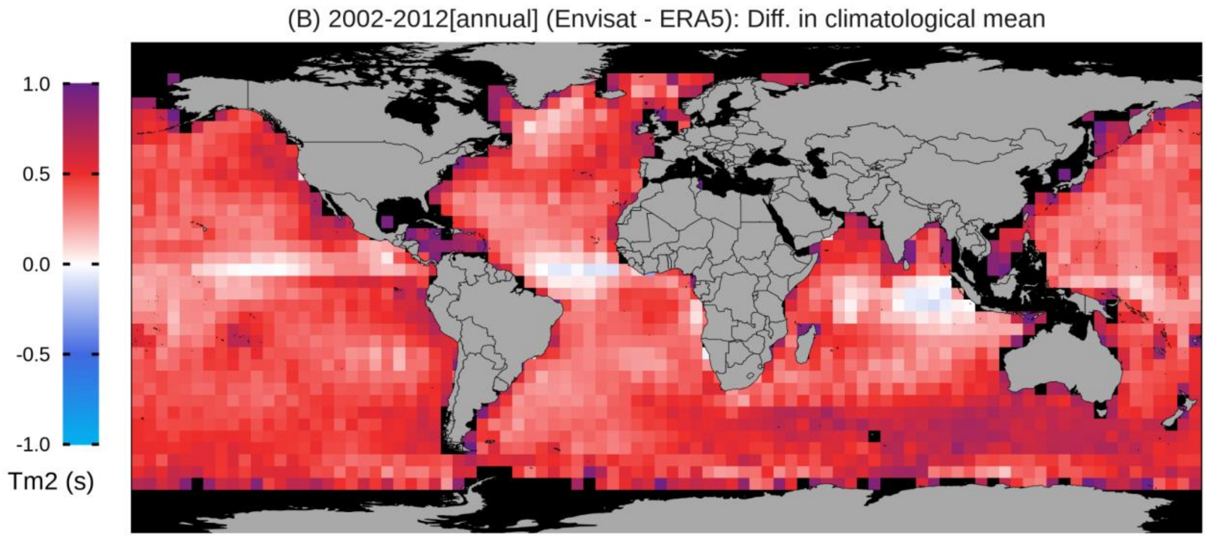

Figure 2.1: Global annual climatological values of T_{m02} from Envisat ASAR (top panel) and mean difference in T_{m02} between Envisat and ERA5 over the same period (bottom panel).

This issue became apparent during Phase 1, when global fields of estimated T_{m02} from Envisat ASAR were intercompared with ERA5. Results of this analysis are shown in Figure 5, where a strong bias can be seen over most of the global oceans. Subsequent analysis, reported in the PVIR, Annex A, revealed that the frequency cutoff value was likely responsible for discrepancy between the two data sources. This type of issue will be particularly relevant to intercomparisons of integral wave parameters performed during Phase 2.

3. Algorithm development (altimetry, S1 SAR) calibration / verification data summary [WP4110]

3.1 Introduction

This PVIR provides a limited independent validation process for new Sea_State_cci CDRs. Typically, CDRs are intercompared and validated against a range of high quality reference data. However, during algorithm training, calibration and verification activities, performed by algorithm development teams under WP2000, a substantial amount of intercomparison between data sources was undertaken. In effect, these have a downstream effect on independent validation activities (WP4000), since data re-use can lead to both repeated work and invalidate independent assessment. Fiduciary reference data for sea state is somewhat limited and so it is important to track data sources that are being used throughout the production process.

A summary of data usage and methods employed by algorithm development teams is provided in Section 3 of the Product Validation Plan, but an updated summary is also provided here for reference. In this section, further information is provided on the calibration of the altimetry L2p CDR and DLR Sentinel-1 processing.

3.2 Level-2 altimetry significant wave height

3.2.1 Use of CMEMS In Situ database

The CMEMS In Situ Thematic Assembly Center (CMEMS INSTAC) is a component of the EU Copernicus Marine Service and its role is to ensure consistent and reliable access to a range of in situ data for service production and validation. For this purpose, CMEMS INSTAC collects multi-source/multiplatform data, and performs consistent quality control before distributing the data in a common format to the CMEMS Marine Forecasting Centres (MFC). The dataset is updated on a yearly basis and can be found at http://www.marineinsitu.eu/. For the validation of nadir altimetry wave data, we have considered all in situ platforms located at a minimum distance of 50 km from the shore. The number of selected buoys vary between 42 and 216, depending on the considered mission and its lifetime. As an example, the locations of the buoys used for the validation of ERS-1 and Jason-2 are shown in Figure 3.1.

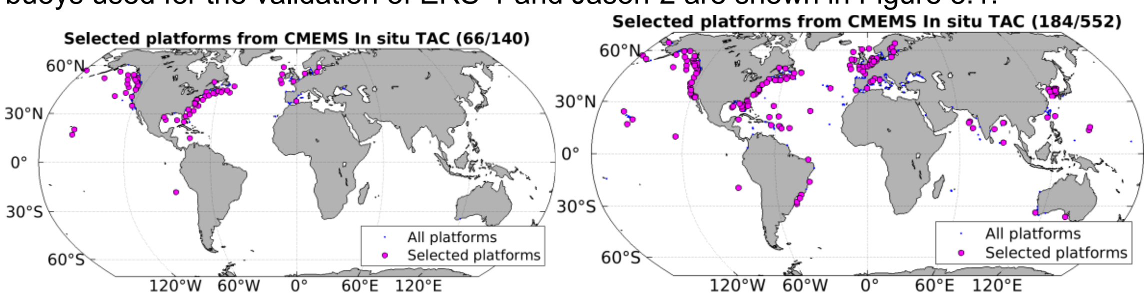

Figure 3.1. Locations of in situ data used for the validation of ERS-1 (left) and Jason-2 (right)

In order to ensure that only valid measurements are selected, a number of tests have been applied:

- Stationarity: rejecting SWH buoy measurements having a constant SWH value over more than 48 hr;
- Location: rejecting SWH buoy measurements over unrealistic position change within a short period of time;
- CMEMS quality check: using the CMEMS native quality flags on time, location and SWH to reject bad or suspect SWH buoy measurements;
- Precision: detecting and rejecting SWH buoy measurements having a precision equal or larger than 0.5 meters;
- Range: rejecting SWH buoy measurements out of the 0-30 metre range.

Match-ups between altimeter and in situ platform measurements were computed within 50 km distance and 30 minute time window. The nearest denoised along-track altimeter SWH record was selected and the in situ SWH observations were smoothed with a 1 hour running average in order to reduce high-frequency variability.

3.2.2. Impact of the bias correction

In order to estimate the impact of the bias correction method on the nadir altimeter SWH records, error metrics (bias, root-mean-squared error, scatter index, correlation coefficient) were computed for each mission (Tables 3.1 and 3.2). These results were computed before and after the bias-correction is performed, using either comparisons between missions at crossover locations or comparisons with in situ data at match-up locations.

3.2.2.1 Comparisons at crossovers

Cross-overs between two altimeter missions are identified when the two altimeter ground tracks cross each other within a 3 hour time window. Denoised SWH records are considered in order to filter out high-frequency variability.

During tandem phases (Topex SideB/Jason-1, Jason-1/Jason-2, Jason-2/Jason-3, Jason-3/Sentinel-6), the two altimeter missions are sharing the same orbit with a slight time delay (less than 1 min) and the so-called “cross-over” data simply correspond to the denoised SWH data recorded at nearly the same location.

The table below summarizes the statistical metrics for 12 pairs of altimeter missions before and after bias correction is applied. As expected, for most mission pairs the bias correction methods reduce the systematic errors between two altimeter missions. The largest normalized bias reduction reaches 13.6% (between ERS-1 and TOPEX sideA) and the mean normalized bias is reduced from 3.5% to 0.6%.

Table 3.1: Error metrics based on comparisons at missions crossovers

Mission 1	Mission 2	NVAL	NBIAS (%)		SI (%)		R	
			Raw	Adjusted	Raw	Adjusted	Raw	Adjusted
ENVISAT-V3	JASON-1E	76690	6,91	0,10	5,32	5,24	0,992	0,993
CRYOSAT-2E	JASON-2D	54338	3,34	0,05	4,53	4,51	0,994	0,994
SARALF	JASON-2D	48353	-1,62	0,14	4,55	4,72	0,994	0,994
SENTINEL-3_A	JASON-3F	31778	8,61	0,11	5,27	5,10	0,993	0,993

SENTINEL-3_B	JASON-3F	31807	8,76	0,11	5,37	5,19	0,993	0,993
JASON-3F	SENTINEL-6	306	-10,00	-2,43	4,40	4,61	0,993	0,994
ERS-1	TOPEX_A	17675	14,63	-1,08	9,79	5,95	0,99	0,99
ERS-2	TOPEX_A	27270	2,37	-3,51	8,45	6,21	0,989	0,99
ERS-2	TOPEX_B	30349	1,06	-0,29	13,86	13,37	0,949	0,953
TOPEX_B	JASON-1E	9364097	8,63	0,03	2,64	2,82	0,998	0,998
JASON-1E	JASON-2D	8705496	-0,82	-0,02	2,12	2,27	0,999	0,999
JASON-2D	JASON-3D	10654786	0,48	0,03	2,20	2,33	0,999	0,999
MEAN		24202452	3,53	-0,57	5,71	5,19	0,990	0,991
MEDIAN		40080	2,85	0,03	4,91	4,91	0,993	0,994

3.2.2.2 Comparison at buoy matchups

An additional verification is carried out by computing error statistics between in situ platform and altimeter records before and after bias correction. These statistics are shown in Table 3.2. The largest normalized bias reduction reaches 17.5% (between Jason-3F and in situ data) and the mean normalized bias is reduced from 1.2% to -0.6%.

Table 3.2: Error metrics based on comparisons at in situ match-ups

Mission	**NVAL**	**NBIAS (%)**		**SI (%)**		**R**	
		Raw	**Adjusted**	**Raw**	**Adjusted**	**Raw**	**Adjusted**
ERS-1-REAPER	2274	-13,82	-5,89	18,44	18,06	0,93	0,93
TOPEXF_TOPEX_A	3755	-3,11	-8,38	17,27	17,16	0,941	0,94
TOPEXF_TOPEX_B	4918	0,56	-0,53	16,87	16,96	0,947	0,946
ERS-2-REAPER	4825	-1,24	-2,74	17,72	17,99	0,932	0,932
JASON-1E	9826	12,28	0,77	15,80	15,64	0,955	0,956
ENVISAT-V3	7058	1,80	-0,70	15,94	15,91	0,955	0,955
JASON-2D	15226	11,72	-0,63	14,12	13,99	0,968	0,969
SARALF	11379	17,50	-1,35	17,79	17,83	0,951	0,953
JASON-3F	5704	24,68	7,18	20,70	20,44	0,938	0,94
SENTINEL-3_A_005	8298	-2,32	-0,19	20,26	19,88	0,94	0,941
SENTINEL-3_B_005	4684	-1,43	0,97	19,82	19,33	0,946	0,947
SENTINEL-6_A_F08	2743	6,20	7,00	28,15	28,46	0,89	0,882
MEAN	6724	4,40	-0,37	18,57	18,47	0,94	0,94
MEDIAN	5311	1,18	-0,58	17,76	17,91	0,94	0,94

3.2 SAR mode [DLR and Ifremer processing]

Sentinel-1 SAR mode data is provided in Sea_State_cci version 4 CDRs. Algorithm development calibration and verification procedures for both the DLR and Ifremer processing methods provided in Sections 3.2 and 3.4 of the Product Validation Plan. No substantial changes have been made to those methods.

In particular, the DLR development process involves the use of both the Météo-France WAve Model (MFWAM) output, based on the IFS-WAM code, jointly developed by ECMWF and Meteo-France. These results are available with a spatial resolution of 1/12 degrees, available from 2016 onwards from CMEMS (2024). Sea state data from a large number of in situ data buoy measurements were used for algorithm verification. All these details are documented in (Pleskachevsky et al., 2022; 2024).

4. Validation of Level-2 altimetry significant wave height [WP4130]

4.1 Data, Scope and Methodology

The CCIv4 altimetry L2p CDR includes the following missions: ERS-1, ERS-2, Topex, Jason-1, Envisat, Jason-2, Cryosat-2, SARAL-Altika, Jason-3, Sentinel-3A/B and Sentinel-6A MF. CCIv4 altimetry CDRs span 1992 to 2023 (complete years). ERS-1, ERS-2 and Topex altimeters represent new additions compared to the version 3 CDR, and extend the record back into the 1990s. Sentinel-3B and Sentinel-6A MF, together with extensions to the other current missions; Cryosat-2, SARAL-Altika, Jason-3 and Sentinel-3A, provide new data up to 2023 (complete year). For 2024, some monthly data is provided depending on availability. Note that long term climatological values of Hs are calculated using complete years only, to avoid the introduction of bias from partial years at the beginning or end of any mission record.

In this section, global data from selected missions is intercompared with ERA5 monthly mean Hs and RY2023 altimetry. In general, climatological average values of Hs are calculated. For the altimetry datasets (CCIv4 and RY2023), both 90th percentile (P90) and standard deviation (sd) of Hs are also calculated. In particular, the periods of the first 10 years of the record (1992 to 2001), represented by ERS-1/2 and Topex, and the last 10 years (2014 to 2023), represented by Cryosat-2, SARAL-Altika, Jason-3 and Sentinel-3A are examined. Noting its importance for multimission intercalibration, and its occurrence during the middle of the CCIv4 record, Jason-2 (2009 to 2018) is individually intercompared with the reference data.

Analysis of CCIv4 data is based exclusively on the variable "*swh_denoised*". Quality control is enforced through filtering "*swh_quality_level*" for "good" data, indicated by a value of 3, against each 1 Hz data point. Data is gridded to 2° x 2° grid cells by taking the median value of all the valid data along each complete track segment within the cell, with a minimum of 5 separate 1 Hz observations. These median values, often referred to as "super observations", are subsequently used to generate climatological summary statistics.

4.2 Intercomparison over Jason-2 period (2009-2018)

4.2.1 Comparisons with ERA5 monthly

Mean Hs for CCIv4 Jason-2 (2009-2018) is intercompared with ERA5 monthly data. JJA and DJF "seasonal" global values are shown in Figures 4.1 and 4.2 respectively. In both datasets, typical climatological patterns for different seasons are apparent, with the most energetic conditions occurring in the lower (JJA) and higher (JFM) latitudes. Little difference can be detected visually but percentage difference is shown in Figure 4.3. Globally, differences are small (up to ~5%), with an overall tendency for CCIv4 to show lower values than ERA5. However, in a few cases, regional differences can reach ~20%. These occur largely in swell dominated regions, sheltered seas and the northern Indian Ocean. While the percentage differences can be large, since average Hs in these regions is often close to 1 m (Figures 4.1, 4.2), absolute differences are quite small (< ~20 cm). It is not unusual to find discrepancies between various reference datasets in these regions, although the exact causes remain unclear. A possible explanation is that low wave heights, dominated by swell, are represented differently due to the specific data source and production methodology.

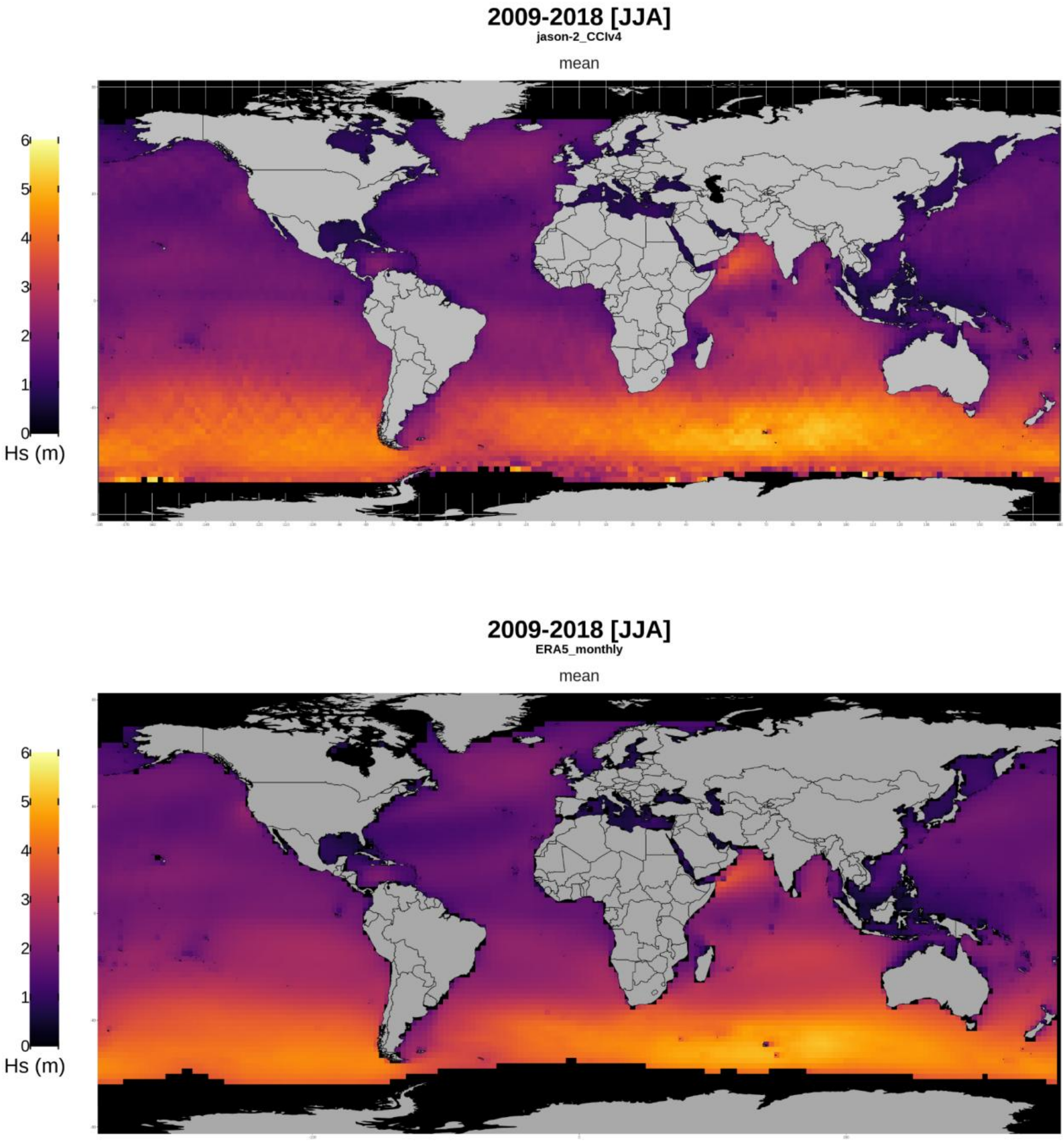

Figure 4.1: Mean Hs for 2009 to 2018 (JJA) on a 2º x 2º grid for Jason-2 from CCIv4 (top) and ERA5 (bottom).

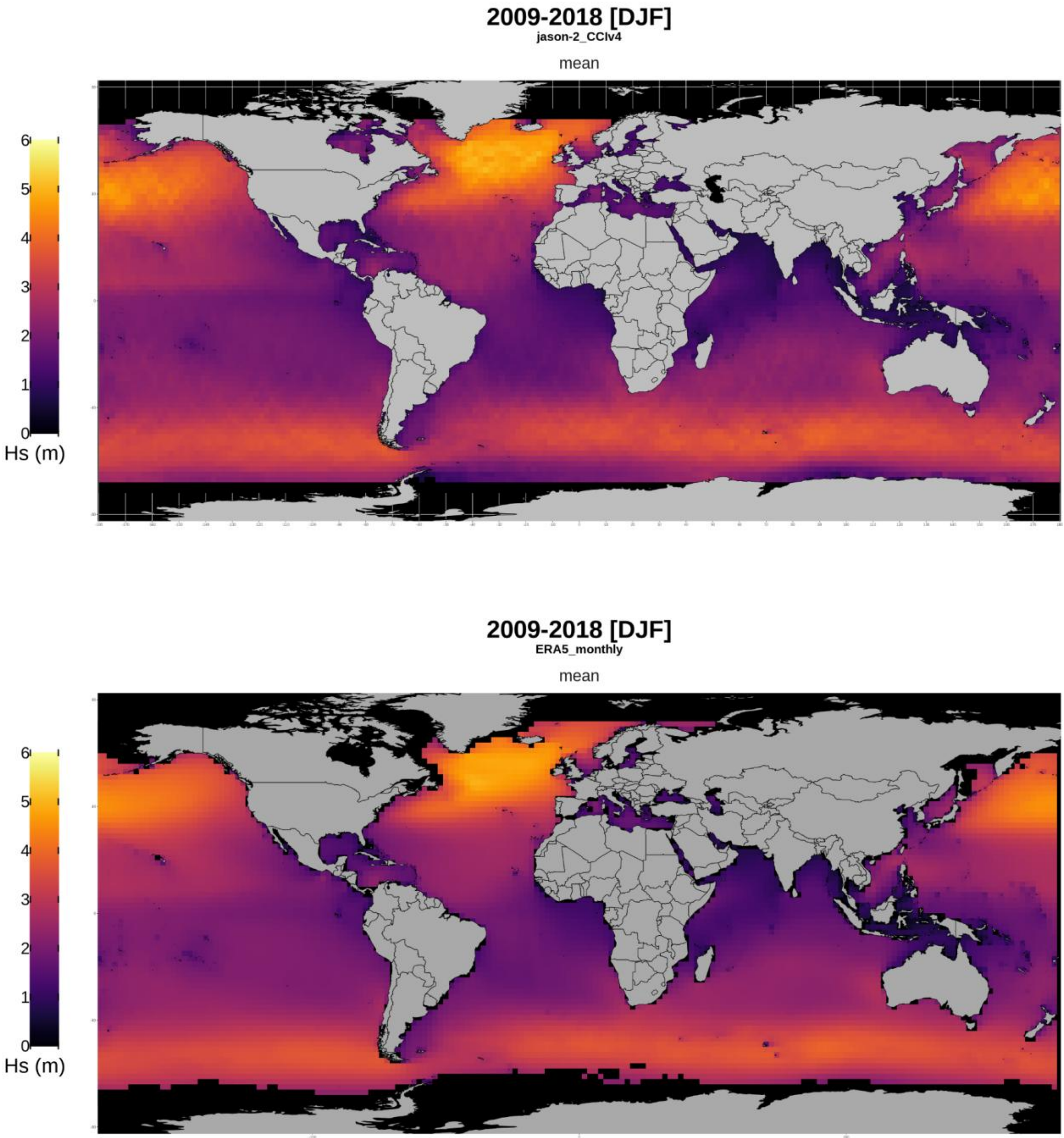

Figure 4.2: Mean Hs for 2009 to 2018 (DJF) on a 2º x 2º grid for Jason-2 from CCIv4 (top) and ERA5 (bottom).

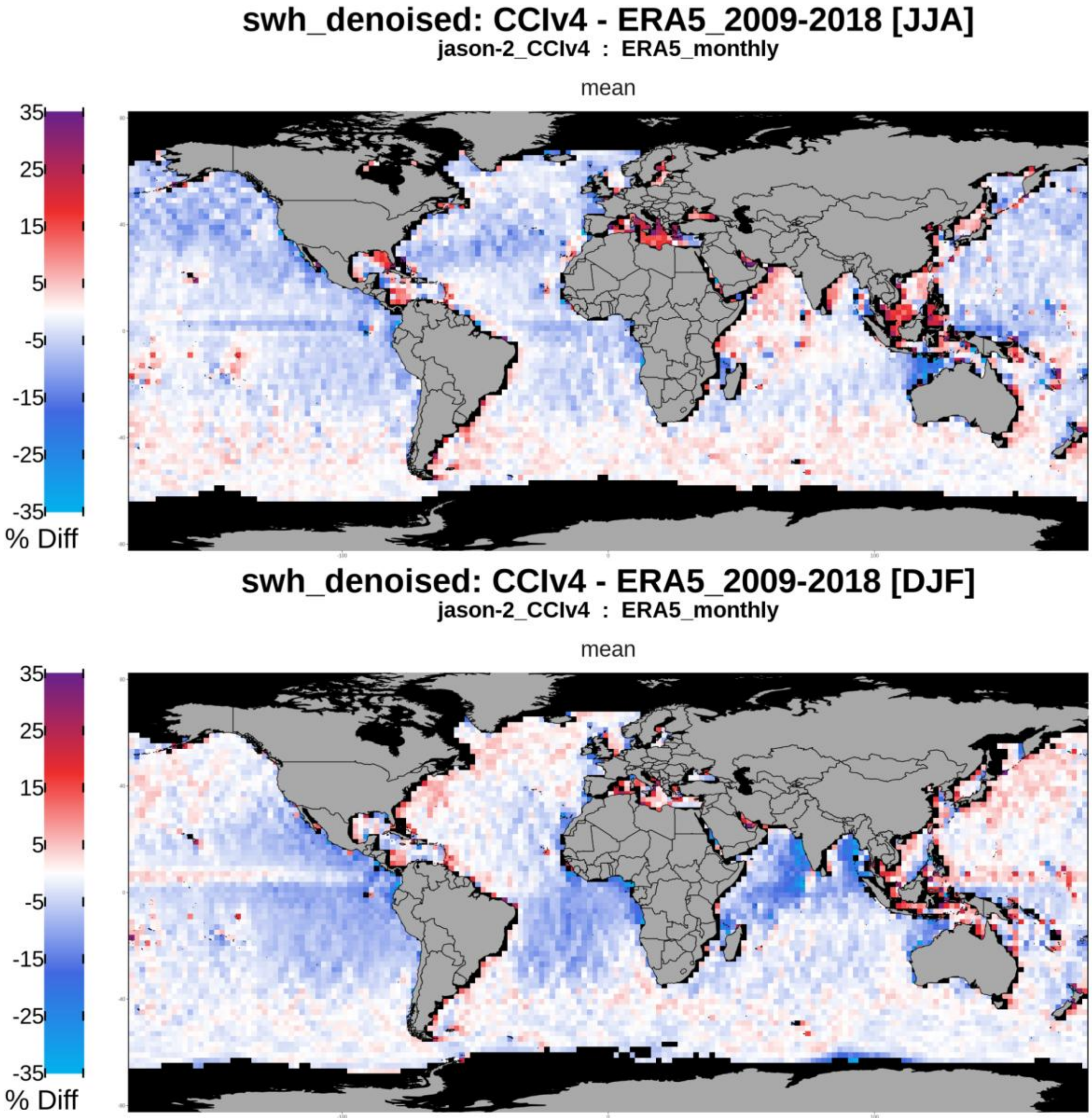

Figure 4.3: Difference in mean Hs (CCIv4 - ERA5) for 2009 to 2018 on a 2° x 2° grid for Jason-2 during JJA (top) and DJF (bottom).

4.2.2 Comparisons with RY2023

Difference in mean Hs (middle panel), P90 Hs (top panel) and Hs sd (bottom panel) for Jason-2 (2009-2018) between CCIv4 and RY2023 is shown in Figure 4.4. Globally, differences in mean Hs are small (up to ~5%) and broadly homogeneous, with an overall tendency for CCIv4 to provide slightly lower values than RY2023. However, a negative difference in the northern Indian Ocean is apparent, somewhat consistent with the difference with ERA5 seen in Figure 4.3. The exact cause remains unclear. Interestingly, for P90 Hs, although CCI shows a tendency for lower values, across the global oceans the difference is highly consistent, with only a small number of regional discrepancies. For sd (bottom panel), CCIv4 shows a tendency for lower values at higher and lower latitudes. This is likely linked to the denoising processes applied to CCIv4 Hs. Seasonally higher values of sd for CCIv4 can be seen in some regions (Pacific and sub-tropics). Reasons for this are unclear.

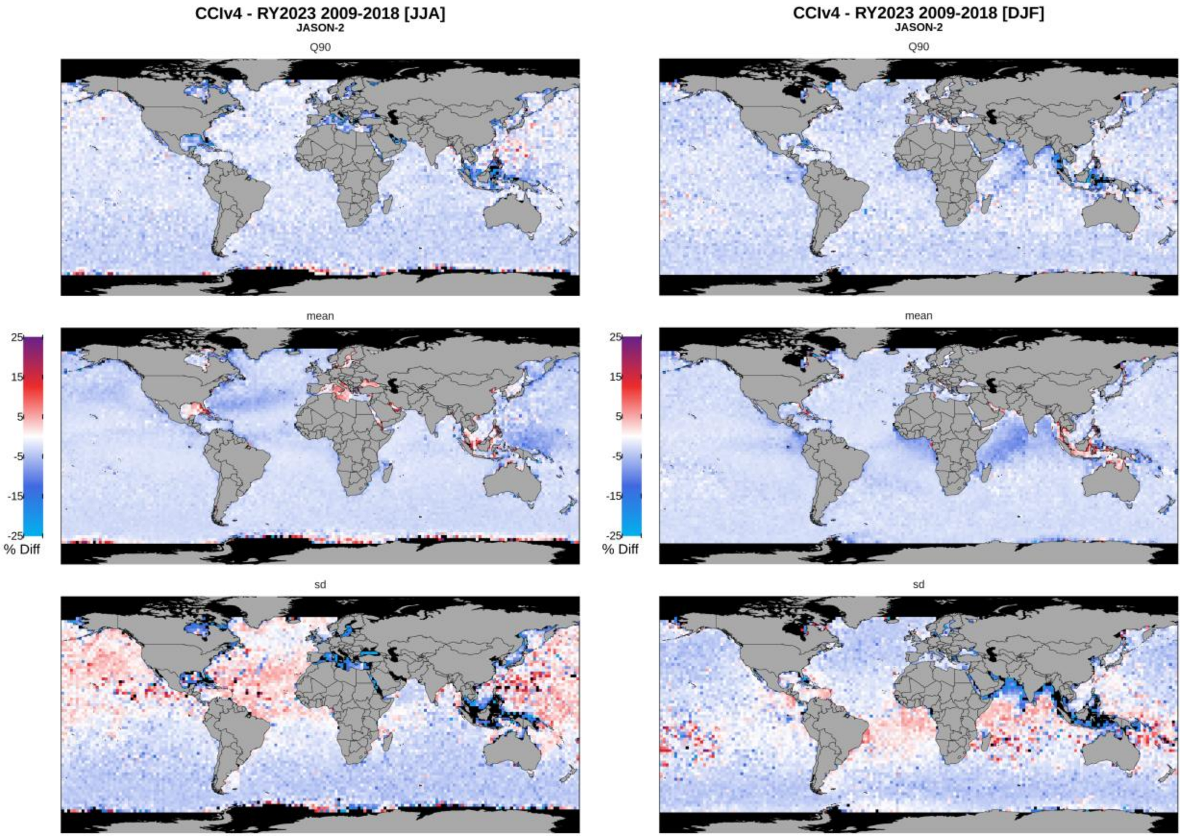

Figure 4.4: Difference in Hs statistics between Jason-2 from CCIv4 and RY2023 for JJA (left) and DJF (right) on a 2^o x 2^o grid, covering 2009 to 2018.

4.3 Intercomparison over first 10 year period (1992-2001)

4.3.1 Comparisons with ERA5 monthly

The earlier (and later) parts of the satellite observational record are important since bias can disproportionately affect the representation of long term Hs trends. Mean Hs for CCIv4 ERS-1/2 and Topex (1992-2001) is intercompared with ERA5 monthly data. Figure 4.5 shows AMJJAS (top panel) and JFMOND (bottom) ”seasonal” global percentage difference. Results are rather similar to those seen for the intercomparison of Jason-2 in Figure 4.3. However, in this case the difference appears to be slightly larger, particularly in swell dominated regions. The northern Indian Ocean is again seen to exhibit the latest discrepancy.

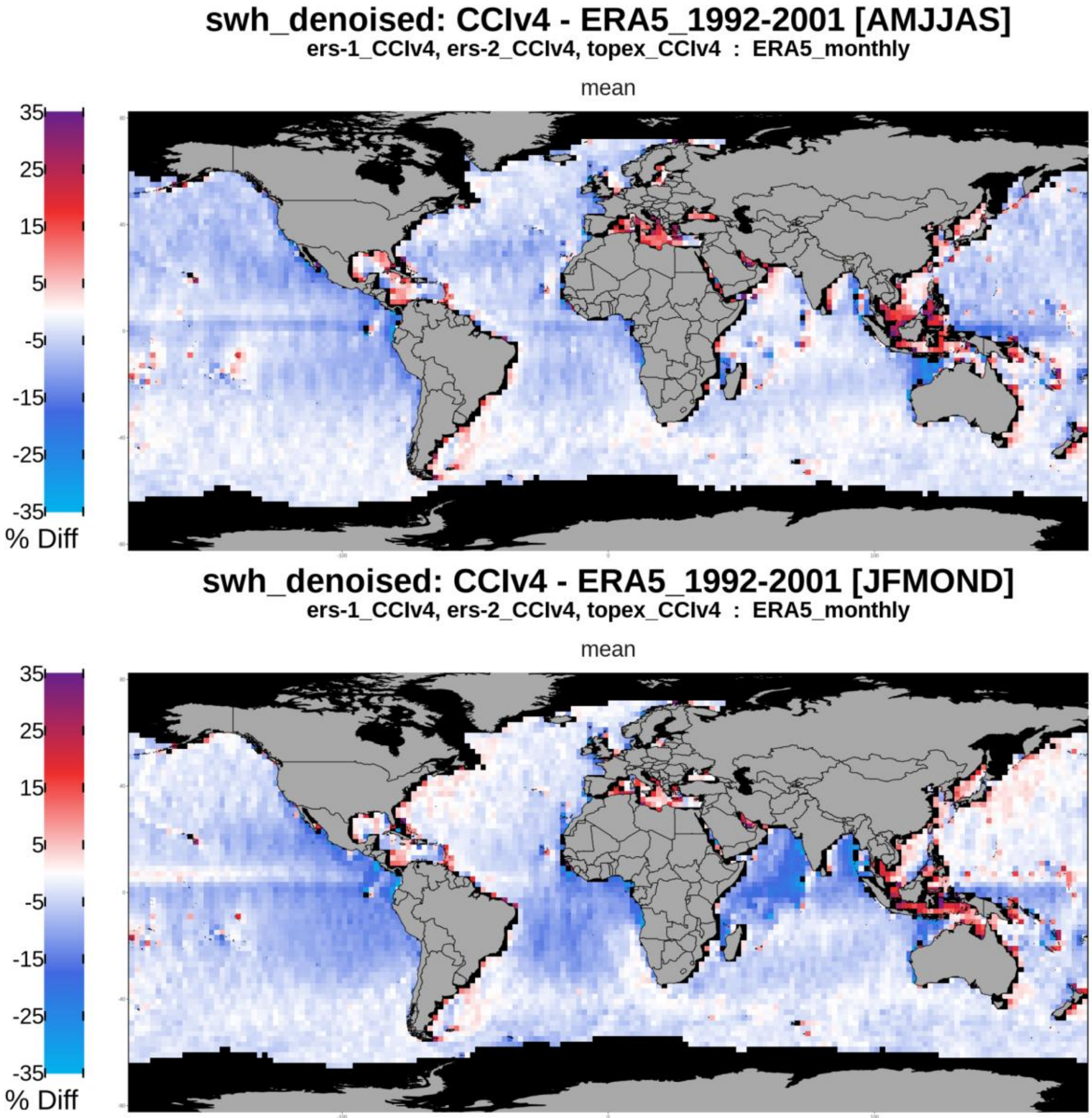

Figure 4.5: Difference in mean Hs (CCIv4 - ERA5) for 1992 to 2001 on a 2° x 2° grid, using ERS-1, ERS-2 and Topex during AMJJAS (top) and JFMOND (bottom).

4.3.2 Comparisons with RY2023

Difference in mean Hs (middle panel), P90 Hs (top panel) and Hs sd (bottom panel) for ERS-1/2 and Topex (1992-2001) between CCIv4 and RY2023 is shown in Figure 4.6. While these results are similar to the comparison with Jason-2, in this case the apparent underestimation seen in CCIv4 compared to RY2023 for mean and P90 Hs is somewhat larger. Globally there is little variation, with a magnitude approaching 10% in most regions. For sd (bottom panel), CCIv4 shows systematically lower values almost everywhere. Again, this is likely linked to the denoising processes applied to CCIv4 Hs.

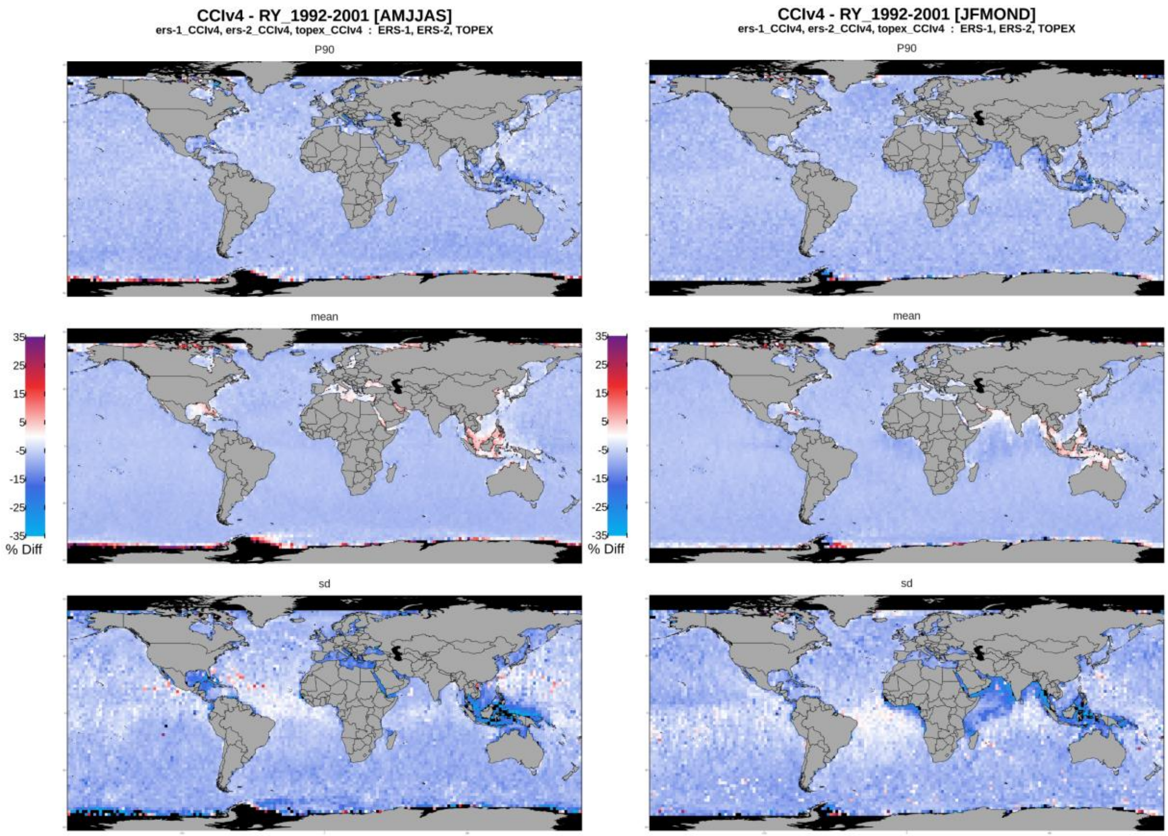

Figure 4.6: Difference in Hs statistics (CCIv4 - RY2023) for 1992 to 2001 on a 2º x 2º grid, using ERS-1, ERS-2 and Topex during AMJJAS (left) and JFMOND (right).

4.4 Intercomparison over last 10 year period (2014-2023)

4.4.1 Comparisons with ERA5 monthly

To complement the comparisons in the first 10 year period, mean Hs for CCIv4, (1992-2001) is intercompared with ERA5 monthly data. Figure 4.7 shows AMJJAS (top panel) and JFMOND (bottom) "seasonal" global percentage difference. Results are similar to those seen for the intercomparison of 1992-2001 (Figure 4.5) although in this case the differences appear to be consistently closer to zero. In some swell dominated regions, differences are slightly larger (~5%), and again the northern Indian Ocean showing the largest difference for JFMOND. More sheltered seas, including the South China Sea and Indonesia, show more variation in difference.

Over most of the global oceans, the closer agreement in Hs climatology in this more recent time period suggests a convergence over time in observations and reanalysis. This might be expected due to increasing, and more accurate, observations, together with a concurrent improvement in modelling. However, regional discrepancies still exist, mostly associated with swell dominated regions.

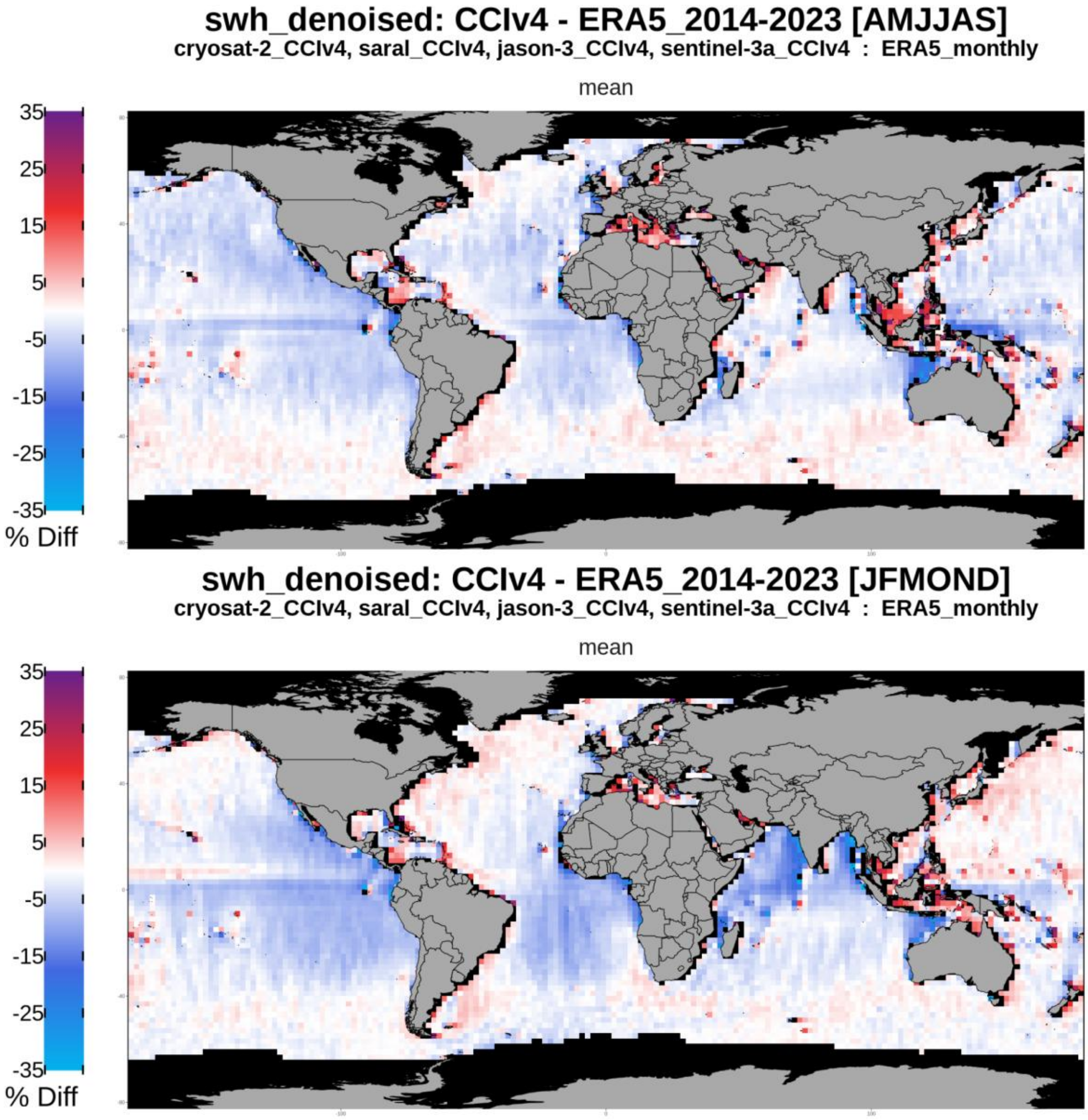

Figure 4.7: Difference in mean Hs (CCIv4 - ERA5) for 2014 to 2023 on a 2° x 2° grid, using Cryosat-2, SARAL and Sentinel-3A during AMJJAS (top) and JFMOND (bottom).

4.4.2 Comparisons with RY2023

The corresponding intercomparison with RY2023 for the most recent 10 year period is shown in Figure 4.8. The same three satellite missions and sensors are used for the comparison. As seen for ERA5, differences in both mean and P90 Hs are remarkably small (< 5%) and globally homogeneous.

Of particular note in this comparison is that the strong regional discrepancies, such as in the northern Indian Ocean and sub-tropics, are largely absent. One possible explanation is that the consistency and accuracy of the most recent mission source data used here is overall much improved compared to earlier missions (such as ERS-1/2), so that both CCIv4 and RY2023 arrive with highly consistent datasets. Only very small differences in calibration can be seen, with CCIv4 slightly lower in value.

Differences in Hs sd (bottom panels) are also mostly very low (< 5%), but there appears to be some cause of a larger discrepancy, possibly associated with a single mission. SARAL has exhibited some historic instability which may be relevant, and possibly filtered out by the CCIv4 denoising process.

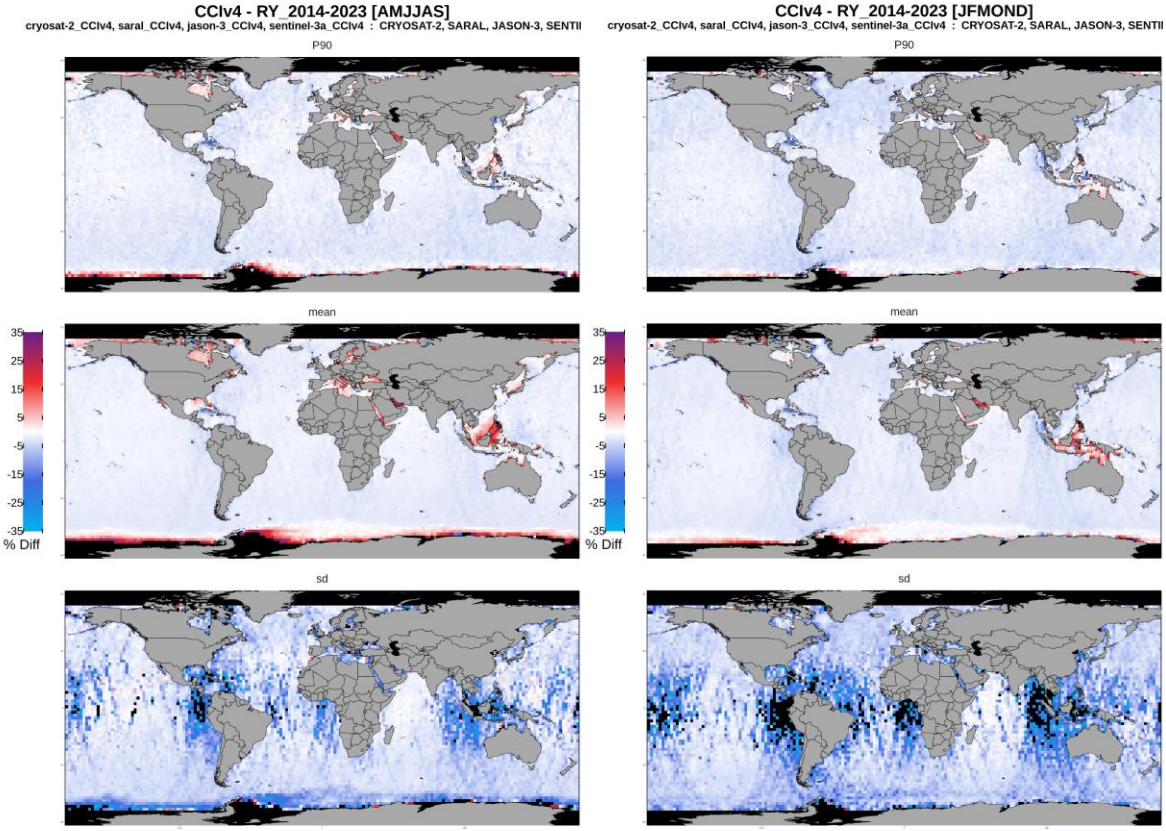

Figure 4.8: Difference in Hs statistics (CCIv4 - RY2023) for 2014 to 2023 on a 2º x 2º grid, using Cryosat-2, SARAL and Sentinel-3A during AMJJAS (left) and JFMOND (right).

4.5 Global sampling for Cryosat-2

Data intercomparisons throughout this section tend to be based on abundant and somewhat uniform global sampling. For example, with the exception of Jason-2, three missions have used over a time period of at least 10 years. However, we draw attention to the fact that some missions exhibit orbital and sampling variation. In particular, Cryosat-2 operates in different altimetry modes. Over most of the global oceans the altimeter operates in traditional low resolution mode (LRM), but over a number of regions, including the European shelf, it switches to synthetic aperture radar (SAR) altimetry mode. This “mode masking” can possibly lead to unexpected data sampling characteristics, and data instability, depending on the time and location of the analysis.

To illustrate this, data sampling for all complete years 2011 to 2023 (JFMOND seasonality) is shown in Figure 4.9 for CCIv4 (top) and RY2023 (bottom). The “box-like” discontinuities in the regular sampling pattern indicate the application of the SAR mode mask. In these regions, little or no LRM data is captured, and so is not included in CCIv4 or RY2023. However, for some SAR regions, the mask is not permanently applied though the mission history, and so at least some data is available. An important consideration therefore, when using Cryosat-2 data in these regions (or subset thereof), is whether a consistency of data is available, and that (e.g. seasonal) bias is not introduced.

Furthermore, in Figure 4.9, both panels are very similar, but with some very small difference in data sampling levels, indicated by small differences in colour. For example, under close scrutiny, one can see that RY2023 shows a slightly larger sample over Europe. This is attributed to different original data sources.

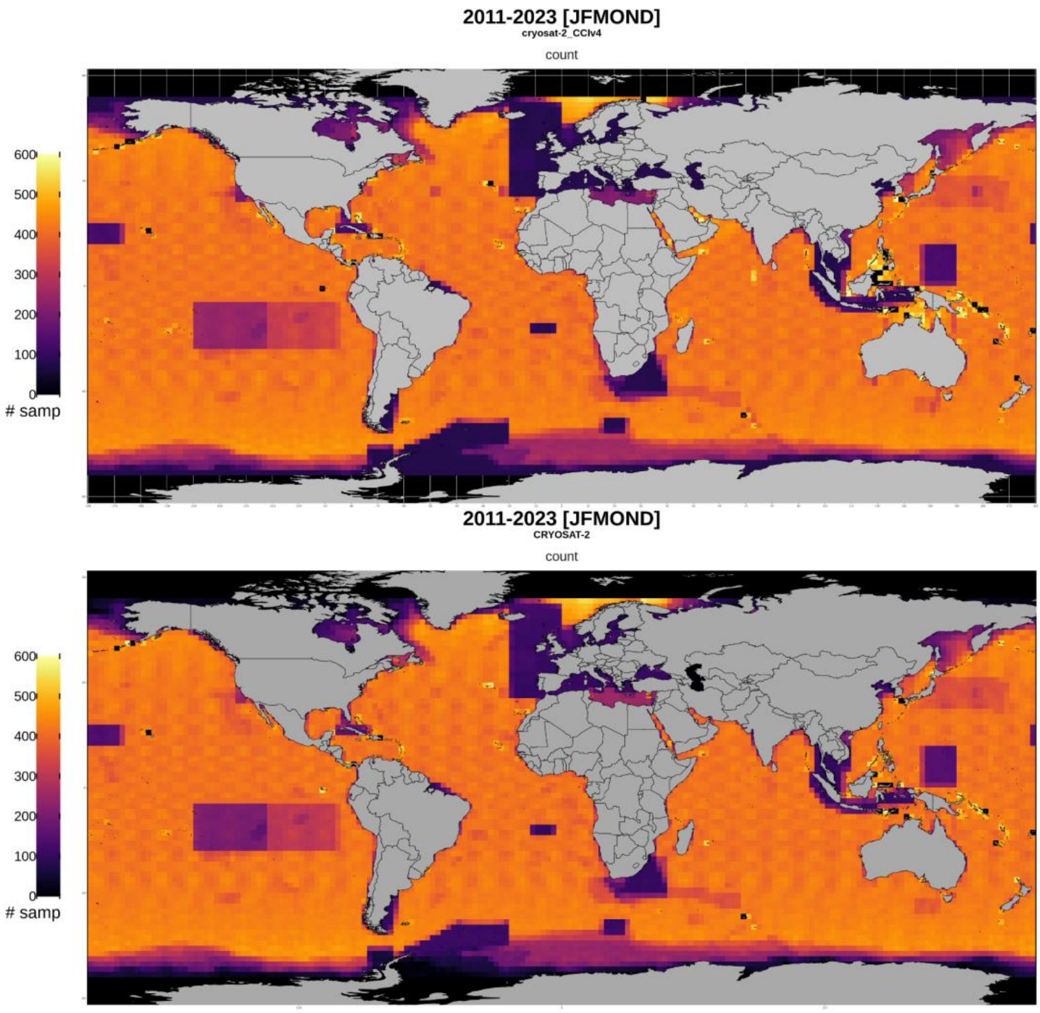

Figure 4.9: Data sample patterns (ONDJFM) per 2° x 2° grid cell for CCIv4 L2p Cryosat-2 (top panel) and RY2023 (bottom panel). Note that the square features are due to the Cryosat SAR-mode mask.

5. Validation of Level-4 significant wave height [WP4120]

5.1 Scope

5.1.1 CCI

The data release for CCIv4 includes an update to the Level-4 (L4) gridded monthly dataset on a global 1° x 1° grid. The dataset follows the same formatting and data structure as version 3. It comprises the following missions: ERS-1, ERS-2, Topex, Jason-1, Envisat, Jason-2, Cryosat-2, SARAL-Altika, Jason-3, Sentinel-3A/B (PLRM) and Sentinel-6A MF. Temporal coverage is from 1992 (complete year) until 2024 (January only).

The L4 gridded product is intended for efficient long term analyses based on monthly summary statistics, including the mean and max observed Hs. More extreme measures of Hs can also be studied, though the use of the threshold exceedance statistics. For example, within each month, the number of individual observations exceeding certain levels of Hs (e.g. at various values between 0.5 m and 10 m) are recorded. These can be used directly, or to generate a coarse estimate of the monthly Hs distribution. However, these data are not considered in this report.

Having already examined global Hs climatologies from the constituent L2p datasets, in this section, long term linear trends are estimated, and intercompared with ERA5, in a way similar to that reported in the PVIR version 3 and Timmermans et al. (2020). Data are regridded to a global 2º x 2º grid, where monthly values are used to fit a linear model to explain the linear trend. For consistency with the PVIR version 3, trends are calculated on seasons JJA and JFM.

5.1.2 Validation reference data

Here, comparisons with the CCI version 1 long term altimetry CDR (1992 to 2017) and ERA5 monthly mean Hs, are provided.

5.2 Long term trend estimation

5.2.1 Trend estimation from CCIv4 L4

Trend estimation is an area of continuing interest and particularly relevant under global warming and climate change. Linear trends can be estimated using annual mean Hs from the L4 product. Timmermans et al. (2020) found little difference between linear regression and the widely used non-parametric “Sen” method (Young & Ribal, 2019; Hirsch et al., 1982).

The PVIR version 3 reported long term linear trend estimates using the version 1 L4 dataset spanning 1992 to 2017. We are now able to update that work with the CCIv4 L4 dataset.

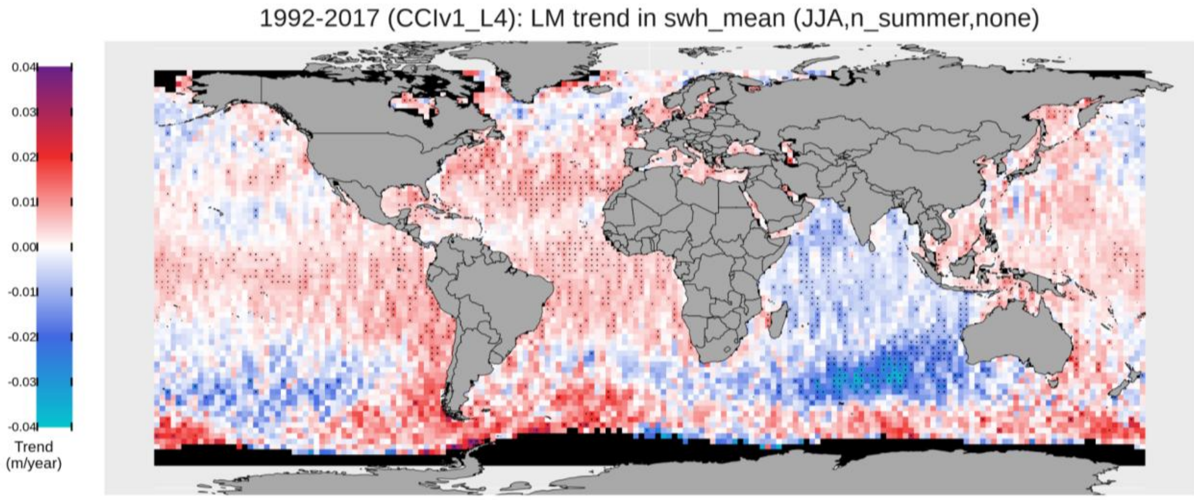

Figure 5.1: CCIv1 L4 mean Hs trend for JJA (1992 to 2017) on a 2° x 2° grid.

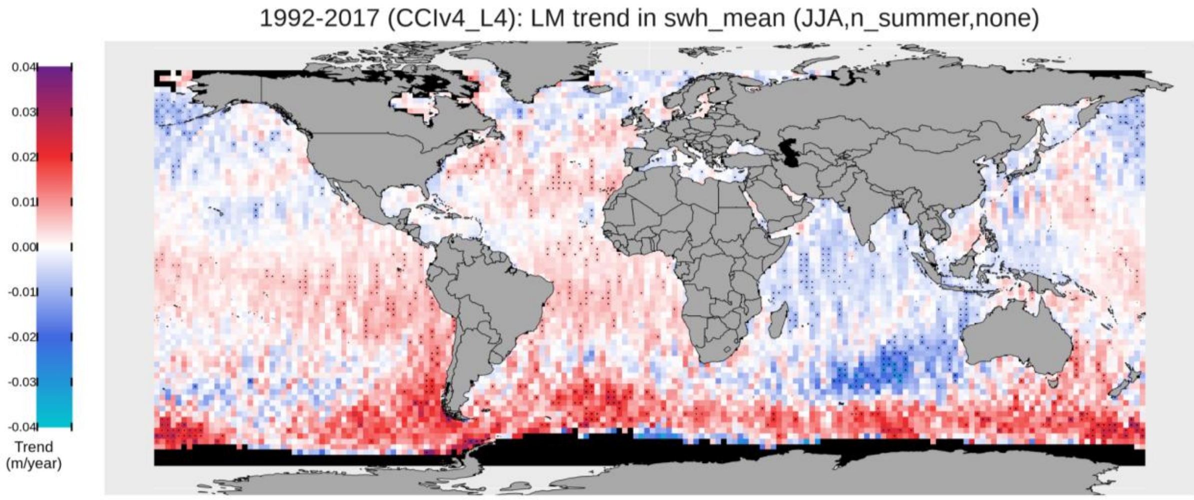

Figure 5.2: CCIv4 L4 mean Hs trend for JJA (1992 to 2017) on a 2° x 2° grid.

Comparison between trends from the CCIv1 and CCIv4 datasets for JJA are shown in Figures 5.1 & 5.2. Differences are small, although overall we see a strengthening of trends globally, with some regional exceptions: in the Atlantic equatorial and lower latitude regions, trends are somewhat reduced (towards zero). These changes are likely due to the CCIv4 recalibration (compared to CCIv1) of earlier missions including ERS-1/2 and Topex. The strongest trends are seen in the Southern Ocean, exceeding 1 cm / year, largely consistent with other findings (Young & Riba, 2019; Casas-Prat et al., 2024).

A similar pattern of change in trends in CCIv4 is also seen for JFM (Figures 5.3, 5.4), in particular, higher latitude (negative) trends are positively increased (compared to CCIv1) and in the tropical Indian Ocean trends now appear more neutral.

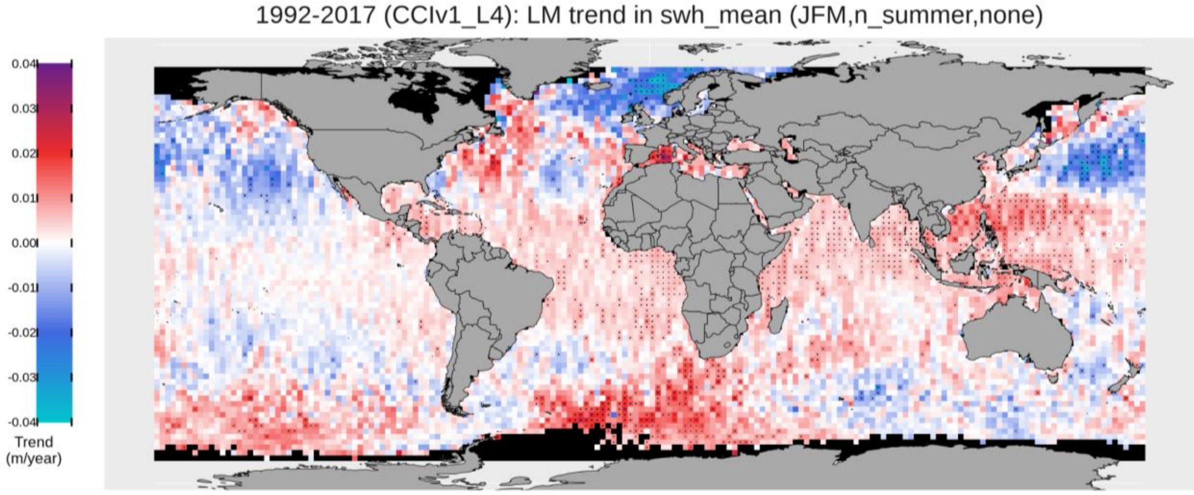

Figure 5.3: CCIv1 L4 mean Hs trend for JFM (1992 to 2017) on a 2º x 2º grid.

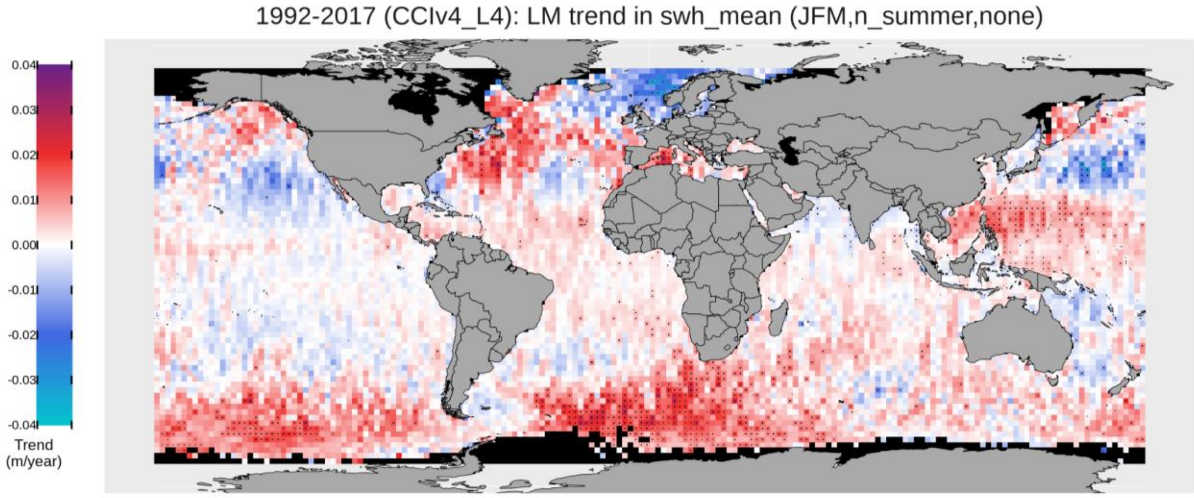

Figure 5.4: CCIv4 L4 mean Hs trend for JFM (1992 to 2017) on a 2º x 2º grid.

The CCIv4 dataset now provides data up to 2023 (complete year), adding 6 years to the existing record. Linear trends, calculated using the same method, are obtained and shown in Figures 5.5 & 5.6.

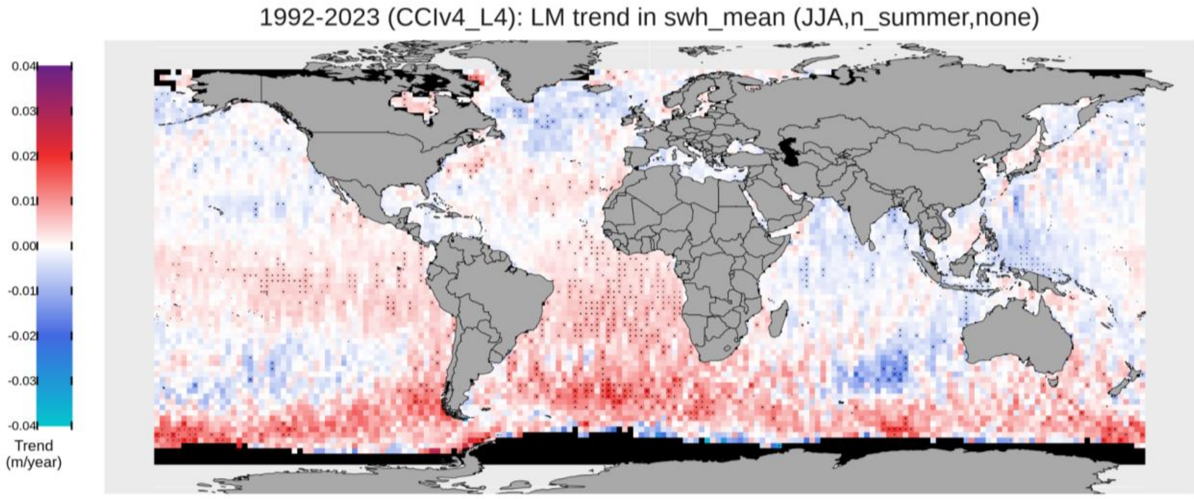

Figure 5.5: CCIv4 L4 mean Hs trend for JJA (1992 to 2023) on a 2° x 2° grid.

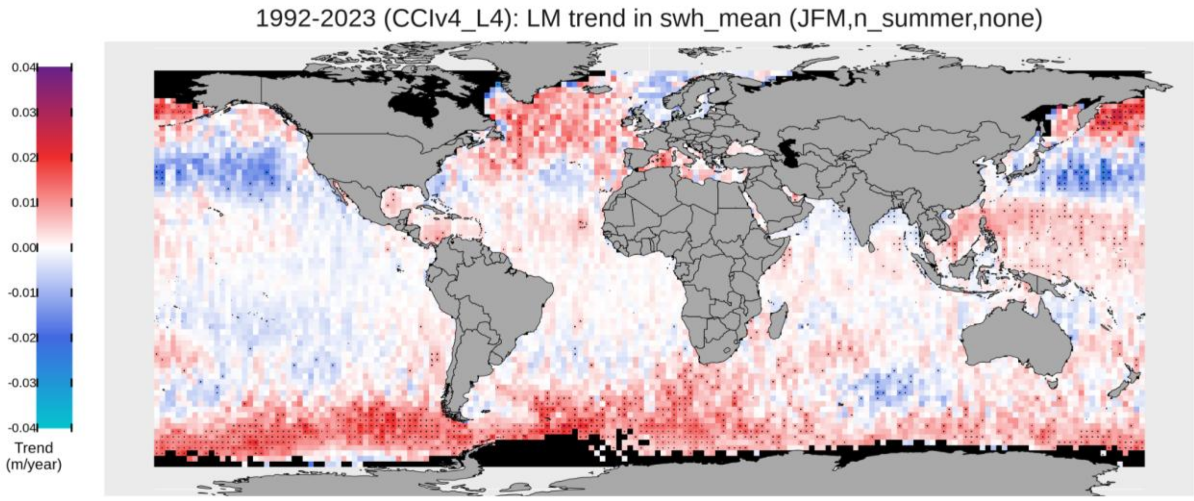

Figure 5.6: CCIv4 L4 mean Hs trend for JFM (1992 to 2023) on a 2° x 2° grid.

The updated results reflect the difficulties in estimating global trends over a relatively short time period in a system of high variability. Updates for both JJA and JFM, now including years 2018 to 2023, both show diminished trend magnitudes (both negative and positive) compared with the earlier evaluations. For JJA in particular, trends appear to be close to zero over most of the globe, with the exception of the Southern Ocean. The region west of Australia now shows a negative trend with a much reduced magnitude. For JFM, regional trend variability in the northern hemisphere remains, vis-a-vis positive trend in the North Atlantic vs negative trend in the North Pacific, although with reduced magnitudes (possibly excepting the North Pacific). The positive trend in the Southern Ocean is also somewhat diminished.

5.2.2 Trend estimation from ERA5 (JFM only)

Linear trends for JFM only are computed for ERA5 over two different time periods. Firstly, we note that issues with ERA5 long term Hs trends have been identified (Timmermans et al., 2020; Meucci et al., 2020), along with a general disparity between trends from reanalyses

(Casas-Prat et al., 2024), whereby instability in the earlier ERA5 record was introduced due to changes in assimilation schemes.

Trends for ERA5 during 1992 to 2023 (JFM) are shown in Figure 5.7, which can be seen to differ somewhat from those over the same period and season from CCIv4 altimetry (Fig. 5.6). In general, trends are lower, particularly in the Southern Ocean.

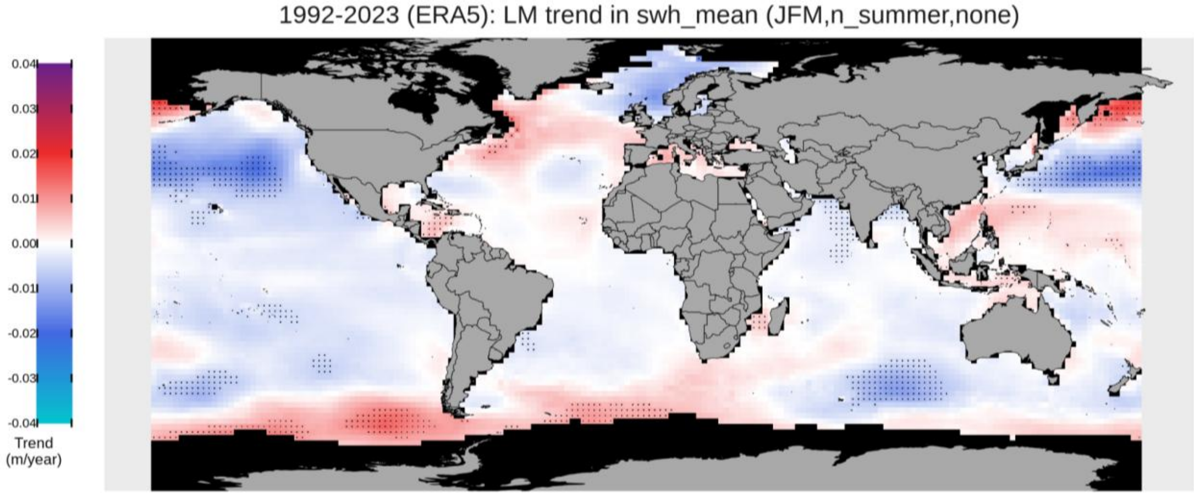

Figure 5.7: ERA5 mean Hs trend for JFM (1992 to 2023) on a 2º x 2º grid.

However, taking trends over the past 20 years, thereby excluding instabilities in the earlier ERA5 record, both datasets can be seen to be in quite close agreement. Trends from 2004 to 2023 from CCIv4 are shown in Figure 5.8, which can be compared with those from ERA5 in Figure 5.9. On inspection, ERA5 may exhibit very slightly lower trends, but the spatial patterns and magnitude of trends are remarkably similar.

These results are consistent with those shown for data from individual missions in Section 4, that over the past decade or so, there appears to be very little difference between various reference data sources (e.g. CCIv4, RY2023, ERA5). This is likely further evidence of steady historical improvement in satellite data accuracy and modelling.

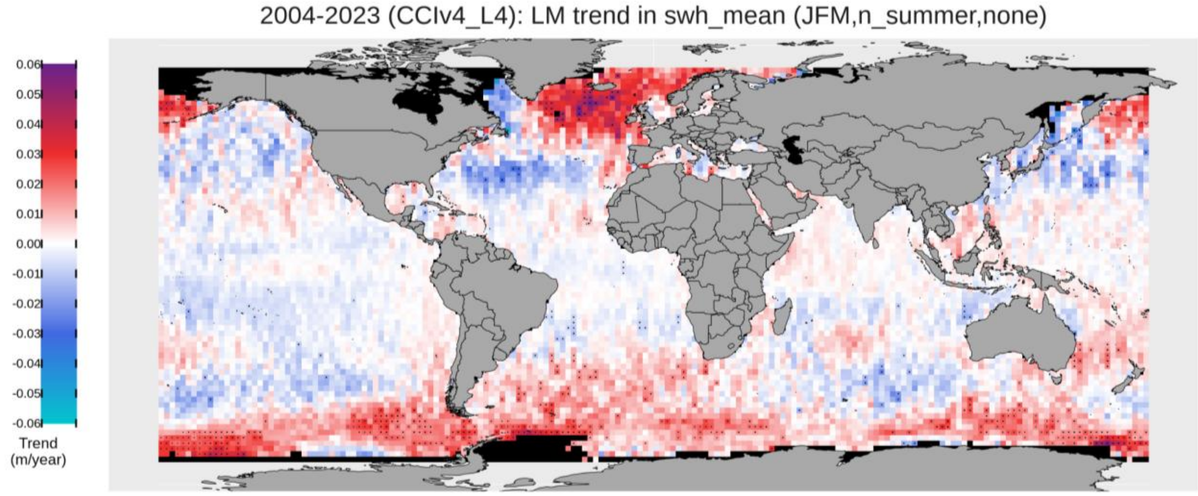

Figure 5.8: CCIv4 L4 mean Hs trend for JFM (2004 to 2023) on a 2º x 2º grid.

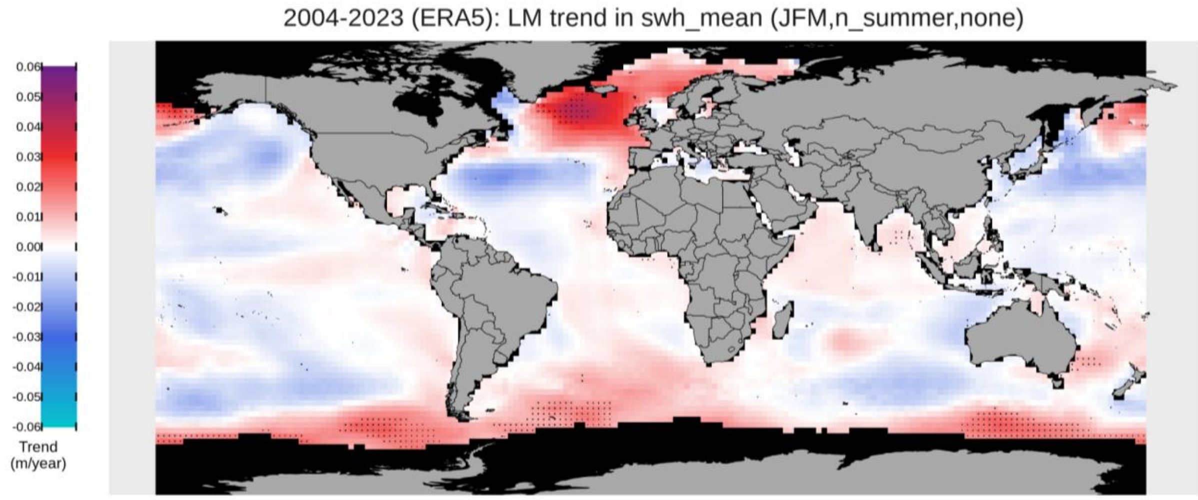

Figure 5.9: ERA5 mean Hs trend for JFM (2004 to 2023) on a 2º x 2º grid.

6. Validation of wave parameters from SAR imaging [WP4140]

6.1 Background

Building on the SAR-derived datasets from Envisat ASAR and Sentinel-1 (S1), produced during phase 1, version 4 CDRs provide additional data from S1 wave mode (WV) and new data from S1 “Interferometric Wide-Swath” (IW) and “Extra-wode” (EW) modes. Two processings of S1 WV are available, from DLR and Ifremer (IFR).

With the failure of S1-B in December 2021, only years beyond 2021 (up to Dec 2024) are available for S1-A. DLR processing is based on the “CWAVE” machine learning method (Pleskachevsky et al., 2022), whereas the IFR processing is based on the “QUACH2020” (Quach et al. 2021). No changes in the algorithmic processing is reported from version 3 CDRs and so results are expected to be largely consistent with those found in the PVIR version 2.

From DLR, a similar range of sea state parameters are available, which includes: Hs total; Hs windsea; three moments of period and partition Hs for two partitions. Ifremer processing provides only total Hs. For reference, the approximate global spatial coverage of the different S1 operating modes is shown in Figure 1 of Pleskachevsky et al. (2022).

Note that, as was the case for CCI version 3 CDRs, no intercalibration between SAR and L2p altimeter datasets has yet been applied in version 4.

In this section, climatologies for SAR parameters including total Hs (DLR and Ifremer), Tm2 and swell primary Hs (DLR) are compared with both the CCI L2p (Jason-3, Cryosat, SARAL, Sentinel-3A) and ERA5 monthly fields.

6.2 Sentinel-1 A/B SAR “Wave Mode” Hs

6.2.1 Long term climatology [DLR processing] compared with CCIv4 altimeter L2p

This section presents the S1 (DLR processing) climatological mean Hs compared with altimeter L2p version 4.

During AMJJAS “season” (Figure 6.1), the northern hemisphere experiences less energetic sea states than ONDJFM, and S1 appears to overestimate, ranging from 5%, up to 10% in places, compared to the L2p. The overestimate at lower wave heights is particularly apparent in swell dominated regions during ONDJFM. Mean Hs in these regions can be as low as 1 m. However, this difference appears to be less pronounced for higher wave heights as seen for P90 Hs (top panels).

In general, for larger wave heights, such as during the Southern Ocean winter (Figure 6.1), agreement between S1 and the L2p is good.

Note also that the difference in Hs standard deviation (sd, bottom panels) frequently exceeds the lower scale bound (-35%) resulting in some black speckled patterns, showing out-of-range values. This is not due to “bad” data, but an issue of constraining the scale for consistent visualisation. This phenomenon is relatively homogenous over the globe. The cause of the large difference in sd, where S1 appears to underestimate with respect to the L2p, remains unclear but may be linked to the nature of the sampling and differences in the respective derivation methods for Hs observations. For example, estimated Hs sd may be artificially low if, for any reason, a sensor were to systematically miss, or underestimate, the peak Hs events. In this case, that would correspond to the SAR missing, or smoothing, the peaks leading to a lower data variance. Unequal sampling between the two analyses could also lead to biases and differences in the representation of Hs variability.

For reference, sample counts (for AMJJAS, 2017-2023) are shown in Figure 6.3. While there is spatial heterogeneity due to the different operational modes of the SAR and altimeters (reported previously in the PVIR version 2), the overall level of sampling between the two SARs (top panel) and three altimeters (bottom panel) is comparable. Therefore, it seems unlikely that sampling alone should lead to such dramatic differences in the Hs sd. However, S1 SAR measurements (single image processing based on a ML methodology) are also derived in a rather different way to the altimeters (smoothed along-track high frequency samples), and thus the interpretation of a sampling comparison may not be intuitive.

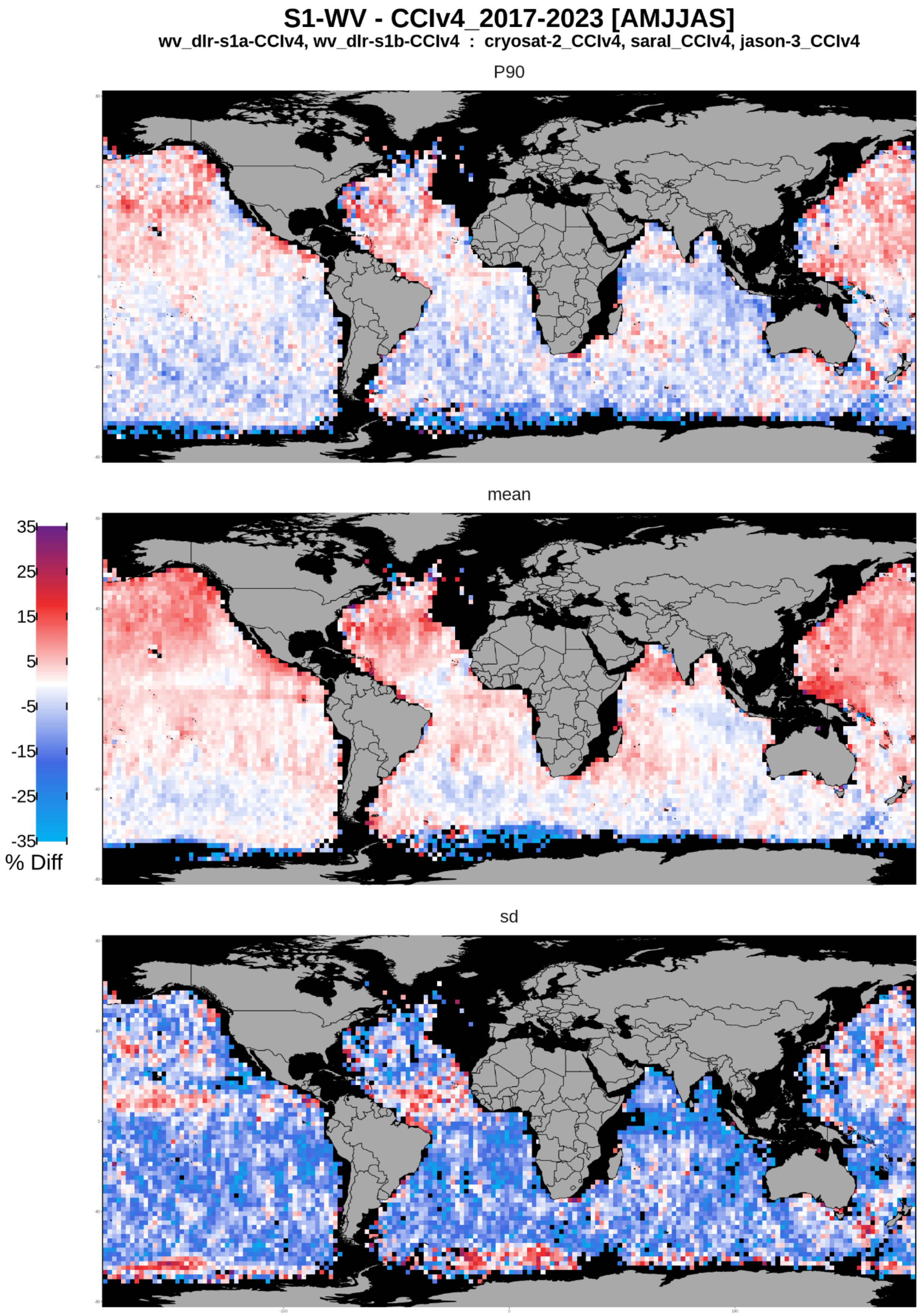

Figure 6.1: Differences in global seasonal (AMJJAS) climatological values (P90, mean and standard deviation) of Hs between CCIv4 L2p and Sentinel-1A/B WV.

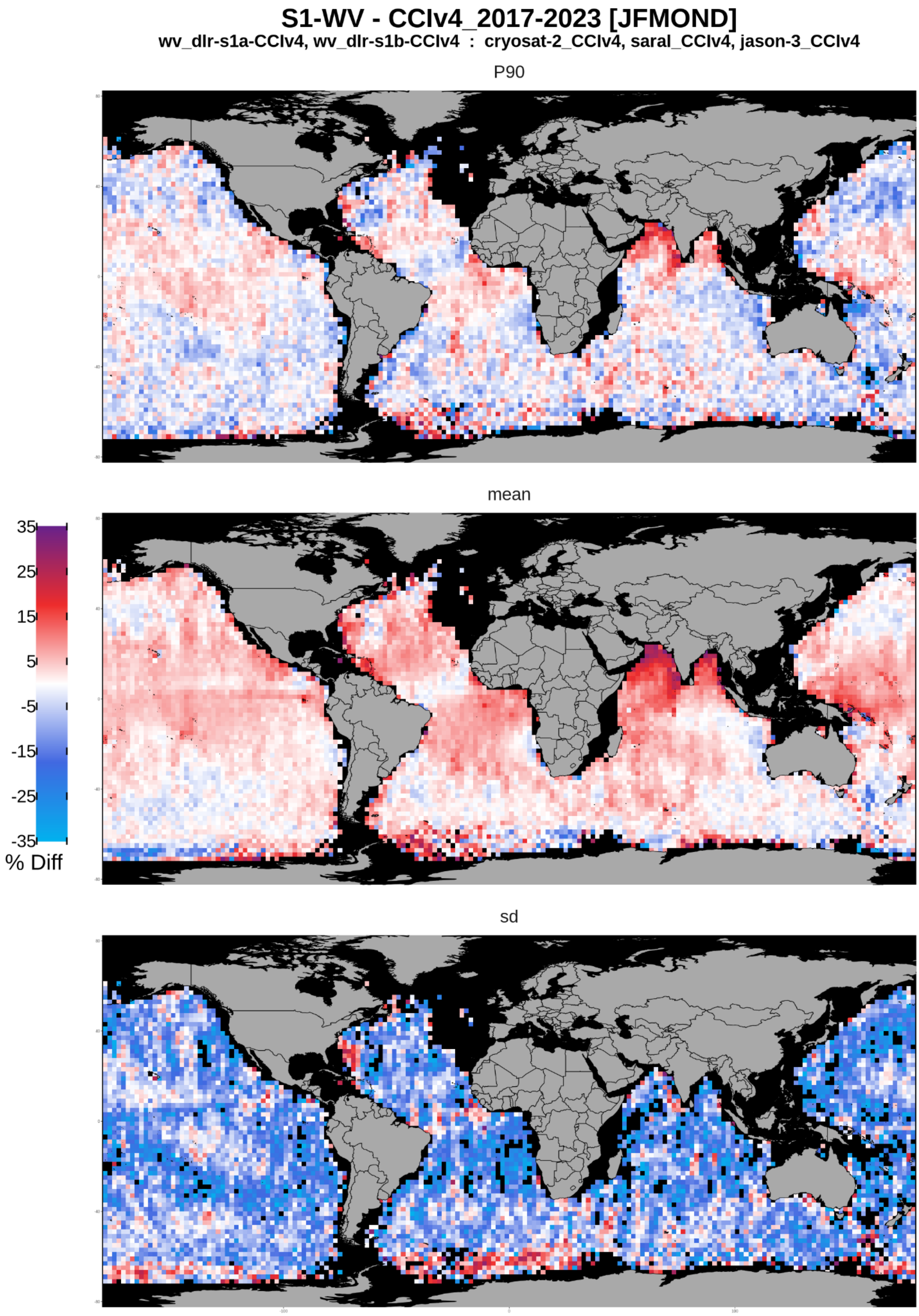

Figure 6.2: Differences in global seasonal (JFMOND) climatological values (P90, mean and standard deviation) of Hs between CCIv4 L2p and Sentinel-1A/B WV.

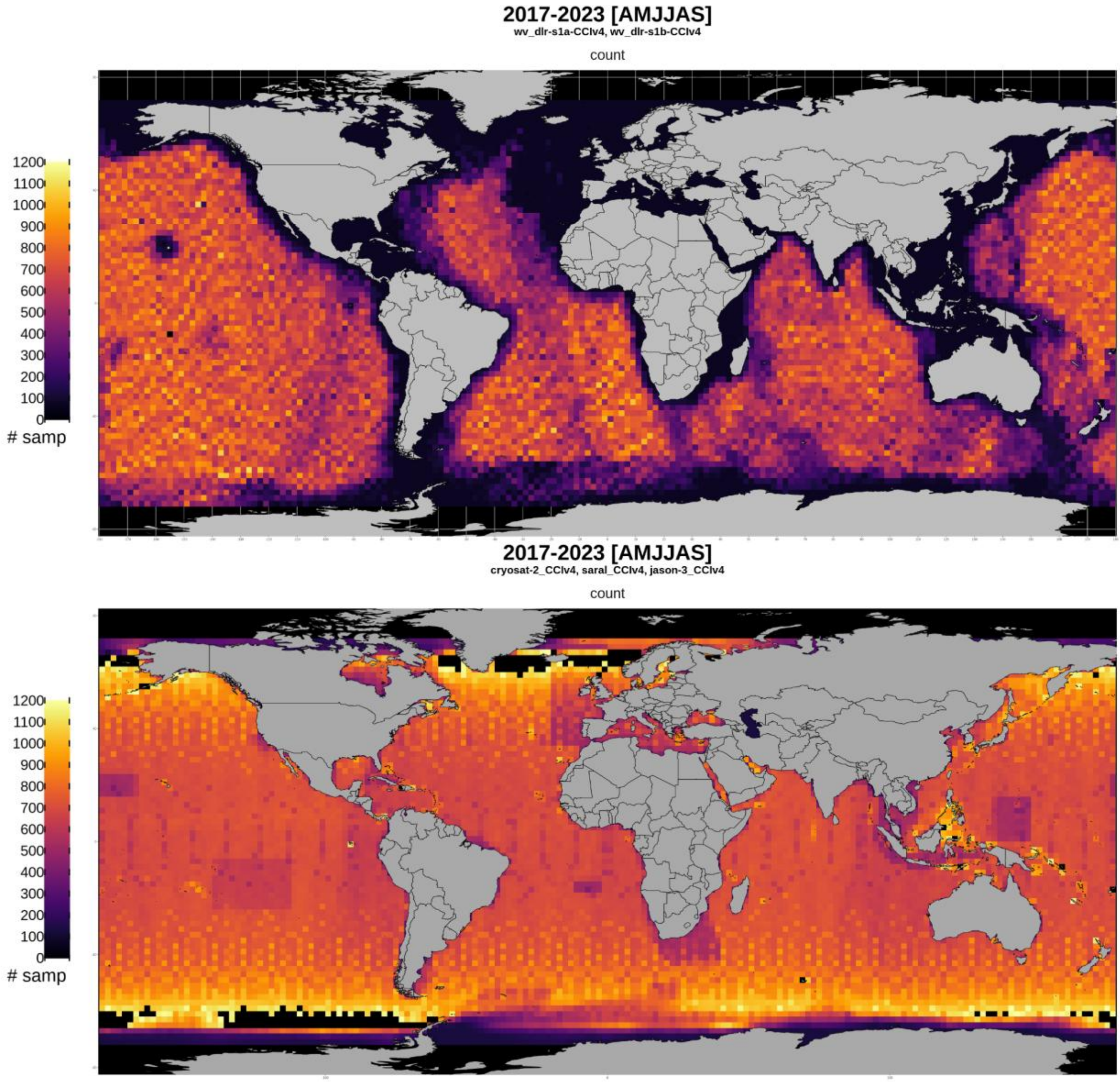

Figure 6.3: Data sample patterns (AMJJAS) per 2 degree grid cell for Sentinel-1A/B WV (top panel) and CCIv4 L2p (bottom panel). Note that the square features in the bottom panel are due to the Cryosat SAR-mode mask.

6.2.2 Long term climatology [DLR processing] compared with ERA5

This section presents the S1 (DLR processing) climatological mean Hs compared with ERA5 monthly fields. As such, only a comparison of the mean climatology is available, shown seasonally in Figure 6.4.

Overall, for both seasons, there is relatively little difference between S1 and ERA5. Globally, the net difference appears to be slightly positive (< ~5%). However, there is considerable regional heterogeneity in differences, with the largest differences associated with sheltered and coastal seas. The northern Indian Ocean and far western Pacific are notable examples.

Some of these differences may be linked to differences in spatial resolution between the two datasets, where S1 WV samples at 20km x 20km compared with 0.5 degree grid cells in ERA5. However, the regions of difference correspond somewhat to those seen for the L2p altimetry CDR (e.g. Figure 6.2), suggesting that the differences are induced in some way by the S1 processing, rather than specific to ERA5.

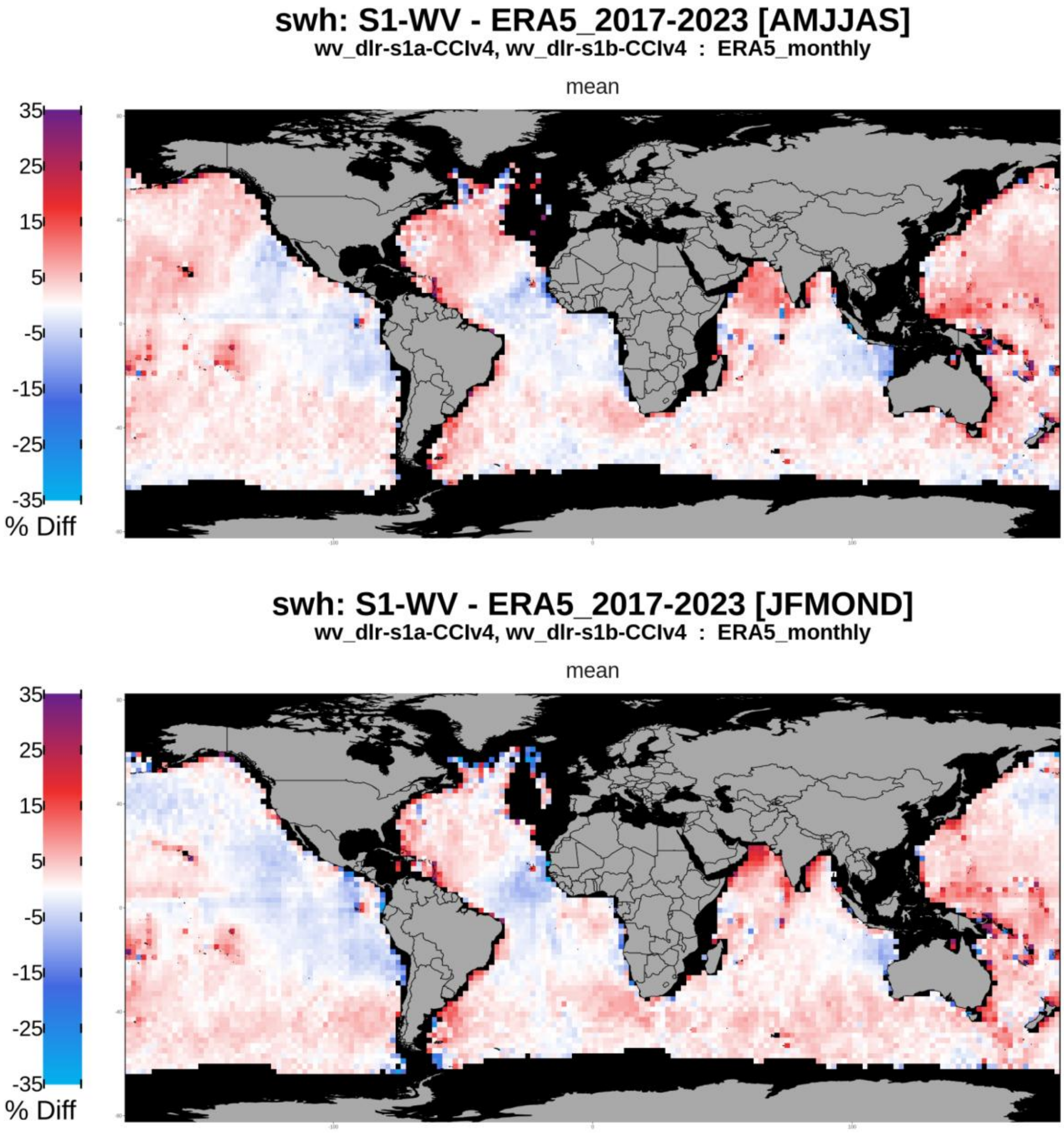

Figure 6.4: Differences in global seasonal AMJJAS (top) and JFMOND (bottom) climatological values of Hs between Sentinel-1A/B WV and ERA5 monthly fields.

6.2.3 Long term climatology [IFR processing] compared with CCIv4 altimeter L2p

This section presents the S1 (IFR processing) climatological mean Hs compared with L2p version 4.

During AMJJAS (Figure 6.5), the equatorial and swell dominated regions show moderate positive mean bias that largely disappears for P90 Hs. However, this grows stronger during ONDJFM (Figure 6.6). This is spatially consistent with the DLR processing, although a stronger effect, notable in the northern India Ocean and far western Pacific. At higher and lower latitudes, where sea states are seasonally stronger, S1 data underestimates with respect to the L2p. This underestimate is quite severe (10% to 20%) at larger wave heights, particularly for the North Pacific summer, and Southern Ocean winter, as shown by the P90 Hs.

Note also that the difference in standard deviation (bottom panels) frequently exceeds the scale range (-35%) resulting in some black speckled patterns in the figures. As for Figures 6.1 & 6.2, this is not caused by “bad” data. As seen for the DLR processing, the large difference in standard deviation may be attributable to a general low bias at large Hs.

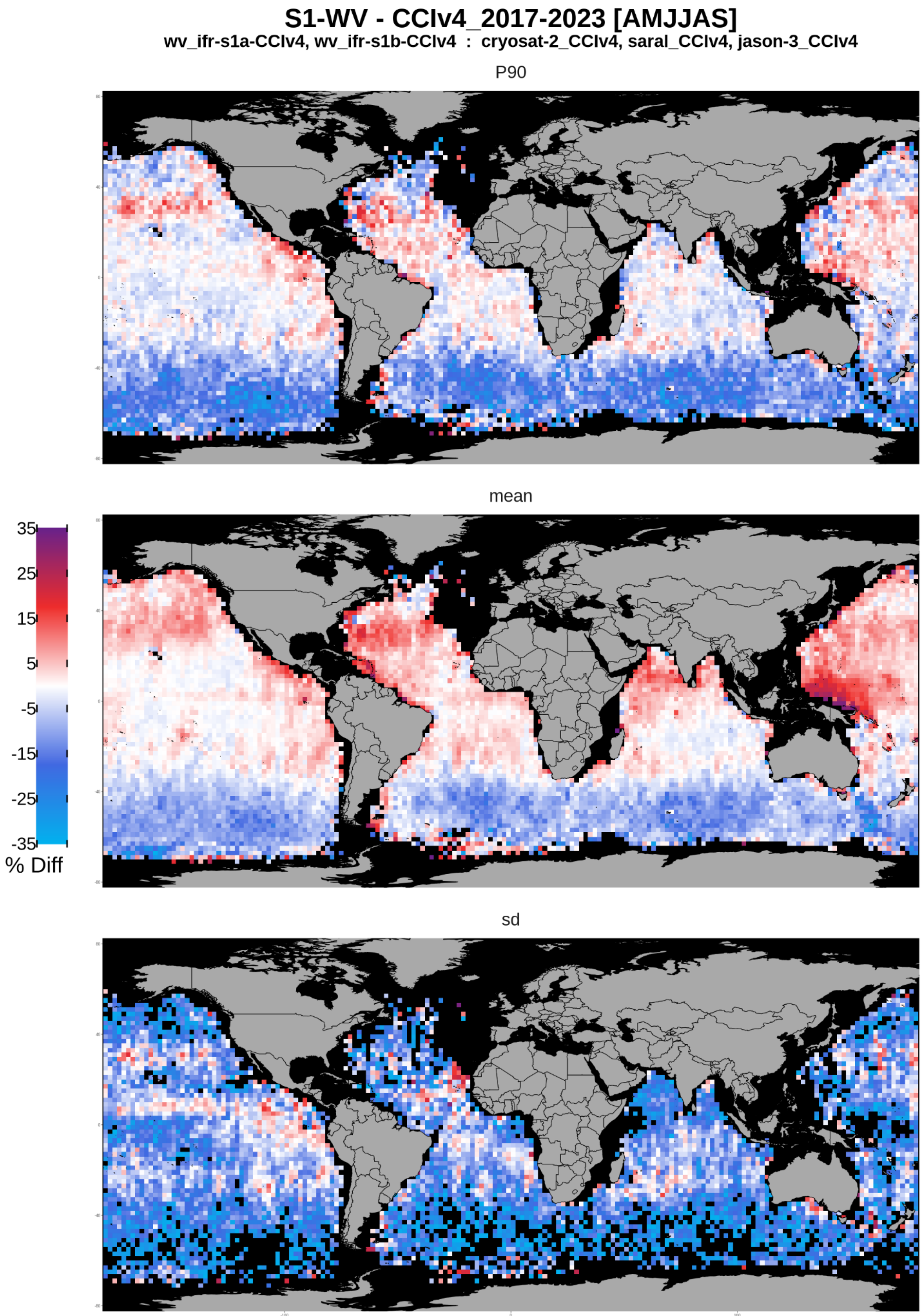

Figure 6.5: Differences in global seasonal (AMJJAS) climatological values (P90, mean and standard deviation) of Hs between CCIv4 L2p and Sentinel-1A/B WV.

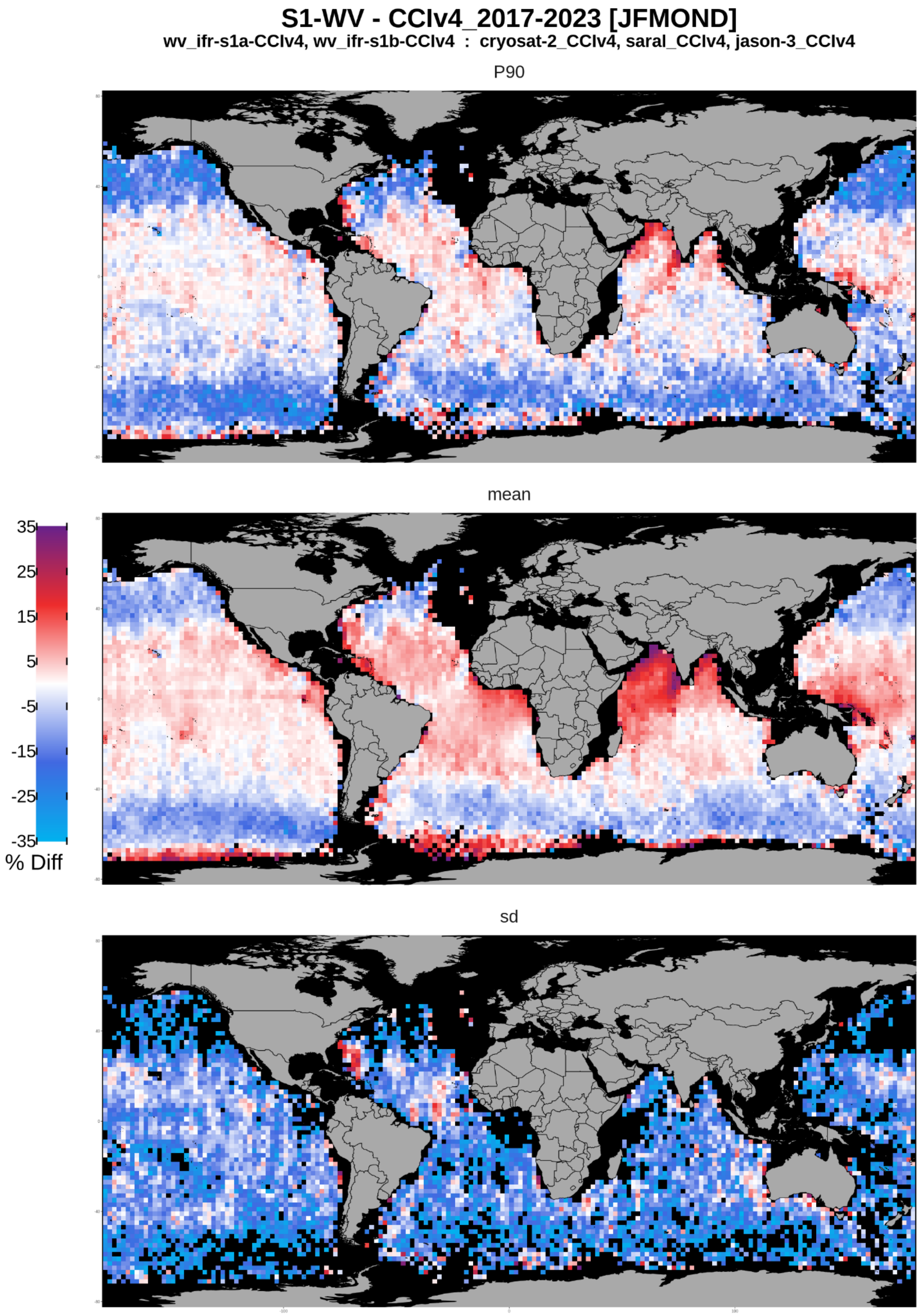

Figure 6.6: Differences in global seasonal (JFMOND) climatological values (P90, mean and standard deviation) of Hs between CCIv4 L2p and Sentinel-1A/B WV.

6.2.4 Long term climatology [IFR processing] compared with ERA5

This section presents the S1 (IFR processing) climatological mean Hs compared with ERA5 monthly fields. A comparison of the mean climatology is shown seasonally in Figure 6.7.

Regional heterogeneity in differences can be seen, similar to the DLR processing, with the largest differences associated with sheltered and coastal seas. The northern Indian Ocean and far western Pacific are notable examples, where the latter difference seems to be somewhat stronger than for DLR processing, approaching 20%.

More striking is the apparent underprediction in the Southern Ocean (AMJJAS) and North Atlantic (JFMOND). This is similar to the comparison seen with the CCIv4 altimetry, and largely expected since the altimetry is in broad agreement with ERA5.

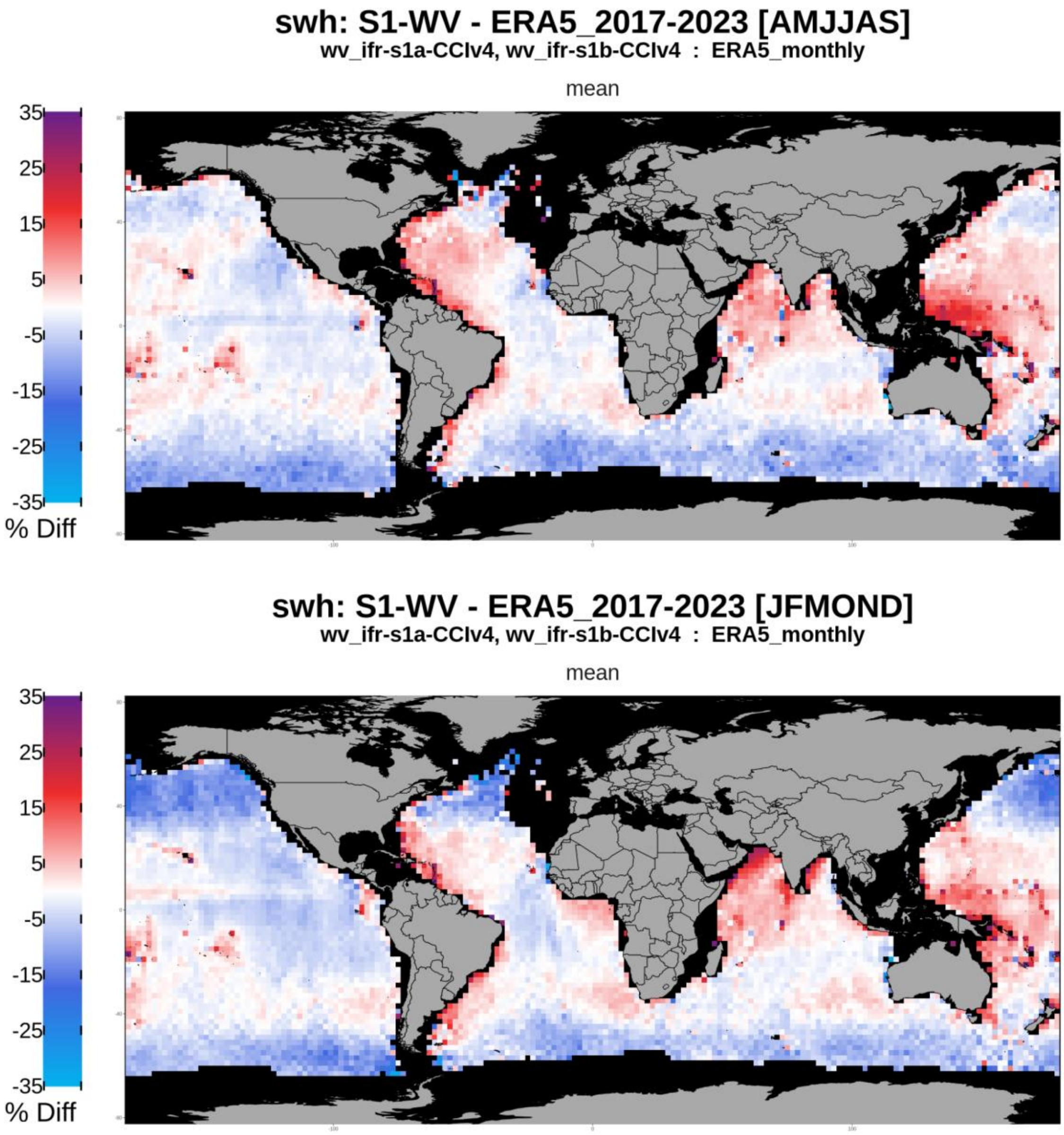

Figure 6.7: Differences in global seasonal AMJJAS (top) and JFMOND (bottom) climatological values of Hs between Sentinel-1A/B WV and ERA5 monthly fields.

6.3 DLR Sentinel-1 A/B SAR "Wave Mode" Sea State Parameters

DLR processing for Sentinel-1 SAR images generates a number of sea state parameters included in the CDR. In this validation, global averages of Tm2 and swell primary Hs are considered.

6.3.1 Long term Tm2 climatology [DLR processing] compared with ERA5

This section presents the S1 (DLR processing) climatological mean Tm2 (see Section 2.1) compared with ERA5 monthly. A comparison of the mean climatology is shown seasonally in Figures 6.8.

Overall, in both seasonal periods, agreement between the two datasets is good. During AMJJAS (top panel), some small regional variations of up to approximately 5% are apparent, which increase slightly during JFMOND. Regionally, these variations coincide closely with those seen for Hs, and are localised to equatorial, swell dominated and sheltered regions.

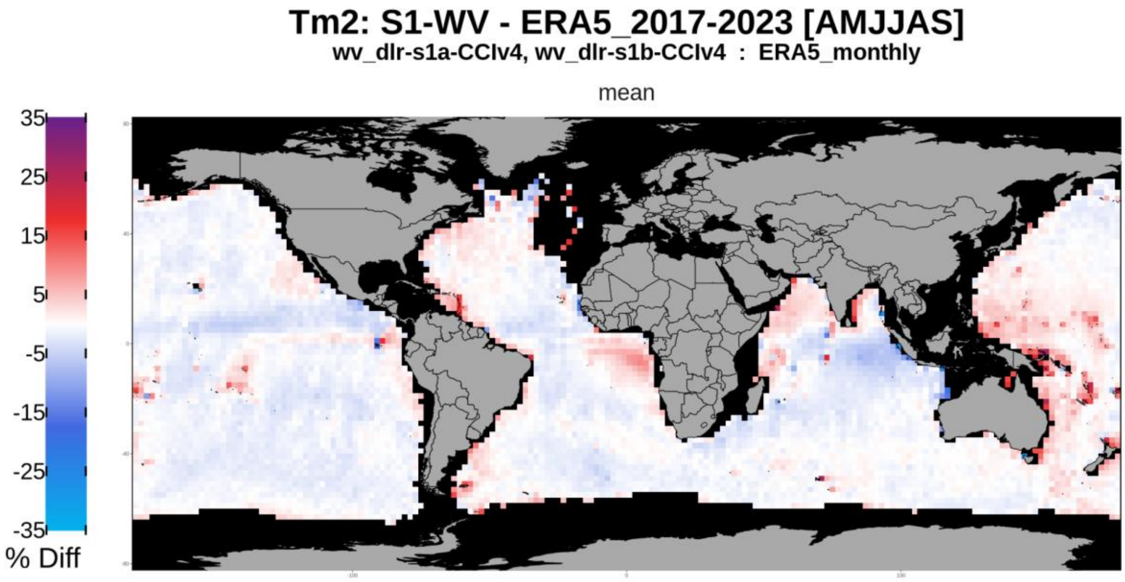

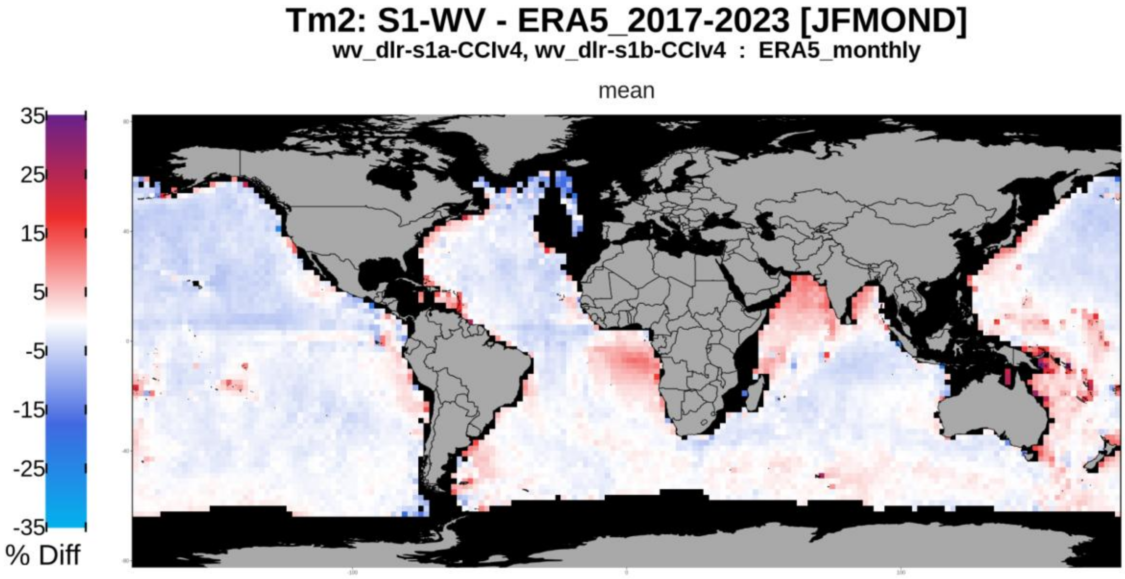

Figure 6.8: Differences in global seasonal AMJJAS (top) and JFMOND (bottom) climatological values of Tm2 between Sentinel-1A/B WV and ERA5 monthly fields.

6.3.2 Long term swell primary Hs climatology [DLR processing] compared with ERA5

This section presents the S1 (DLR processing) climatological mean swell primary Hs compared with ERA5 monthly data. Figure 6.9 shows the results for AMJJAS (top panel) and JFMOND (bottom panel). Interestingly, distinct regions of agreement and disagreement are apparent. In both seasons, good agreement can be seen in the higher and lower latitudes. However, disagreement, exceeding 20% in some locations, is apparent in the sub-tropics, particularly in the Atlantic and Indian Oceans. Both spatially, and in magnitude, the discrepancy is similar in both seasonal periods. We speculate that the areas of strongest discrepancy may be associated with the lowest values of swell Hs, but secondary well systems may be relevant, and further investigation is needed.

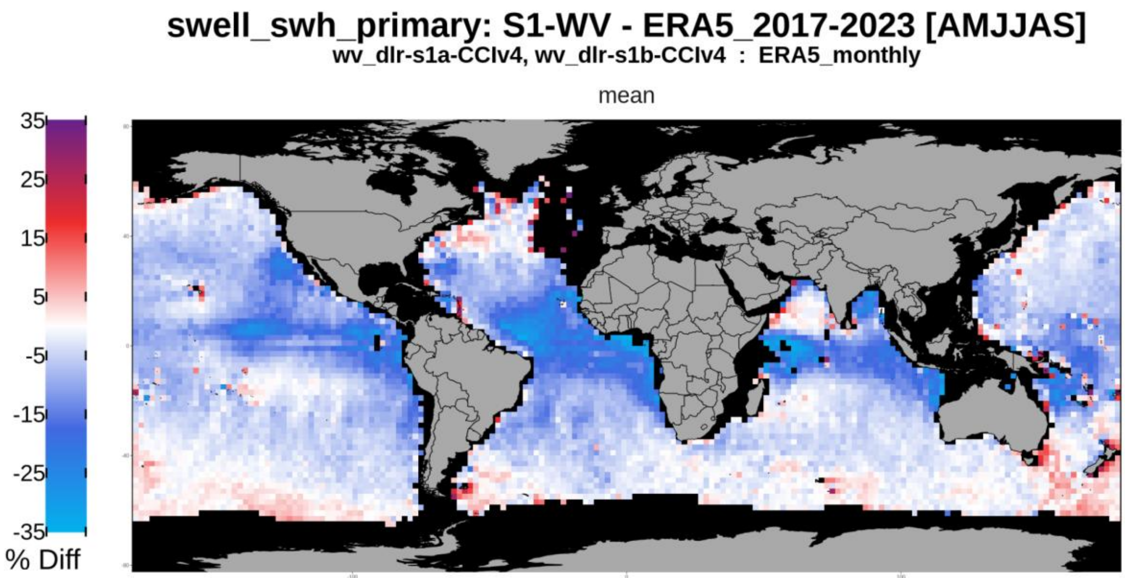

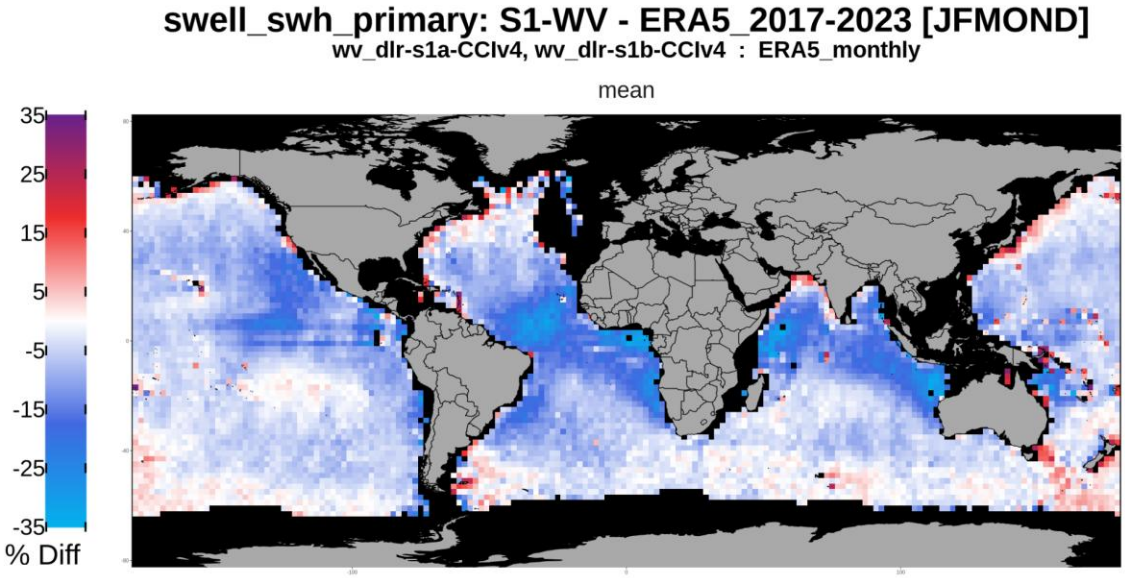

Figure 6.9: Differences in global seasonal (JFMOND) climatological values of swell primary Hs between Sentinel-1A/B WV and ERA5 monthly fields.

6.4 DLR S-1 A/B SAR Interferometric Wide-swath Mode Sea State Parameters

Data from Sentinel-1 SAR "Interferometric Wide-swath Mode" (IW) is a new addition to the Sea_State_cci CDRs. Like S1 WV data, sea state data generation is based on the DLR "C-WAVE" processing algorithm. Notably, however, IW mode provides data over the entire image domain, giving rise to abundant spatial information within each image. This differs from S1 WV, based on smaller images, since only one estimate of local wave parameters is generated per image. In this section we provide an overview of the characteristics of this CDR, and intercompare with the CCIv4 altimetry and ResourceCode high resolution wave hindcast (see Section 2.3.1).

Similar to wave mode (WV), DLR processing for Sentinel-1 SAR IW images generates a number of sea state parameters included in the CDR. In this validation, global averages of total Hs, together with Tm2 and primary swell Hs are considered. Be aware that for version 4, no intercalibration has been performed between SAR and altimetry CDRs (for Hs). This is anticipated in later versions.

6.4.1 Data structure

S1 IW mode captures sea surface observations in images that span approximately 250 km x 250 km of ground coverage—far larger than the 20 km imagettes captured in WV mode. Although the resolution is reduced with respect to WV, images may be processed to provide wave parameters on a grid within each image. For the CCIv4 S1 IW CDR, a grid of ~5 km within each image is used. Images are captured every ~25 s along-track. As such, the CDR comprises around 750,000 imagettes, each providing a grid of approximately 35 x 50 cells for each wave parameter. This is a substantially larger dataset than the equivalent from an altimeter.

Some data "snapshots" captured over the U.K. in January 2020 are shown in Figure 6.10, although note that each descending strip of images is separated by approximately 48 hours.

The spatial structure of the Hs can be seen within each snapshot, and the spatial gradient in Hs, approximately from west to east, corresponds to the prevailing wind conditions for the U.K. winter. The sheltering effect of the land can be seen on the east coasts.

Only data from images from the descending passes of S1A are shown in Figure 6.10, while the location of some “interleaved” passes are indicated by white outlines. No data from ascending passes is shown, nor are data from S1B. While the density of imaging varies geographically due to S1 operational mode switching (see e.g. Figure 6.13 for global counts), in some areas, such as the U.K. and European shelf, data density can be high. In addition to Hs fields, “swell primary Hs” fields for the same “snapshots” over the U.K. are shown in Figure 6.11. Note that the wave height scale is reduced to a maximum of 5 m, and that a large difference in the western and eastern sides of the U.K. indicates the absence of swell in the North Sea compared to the Atlantic.

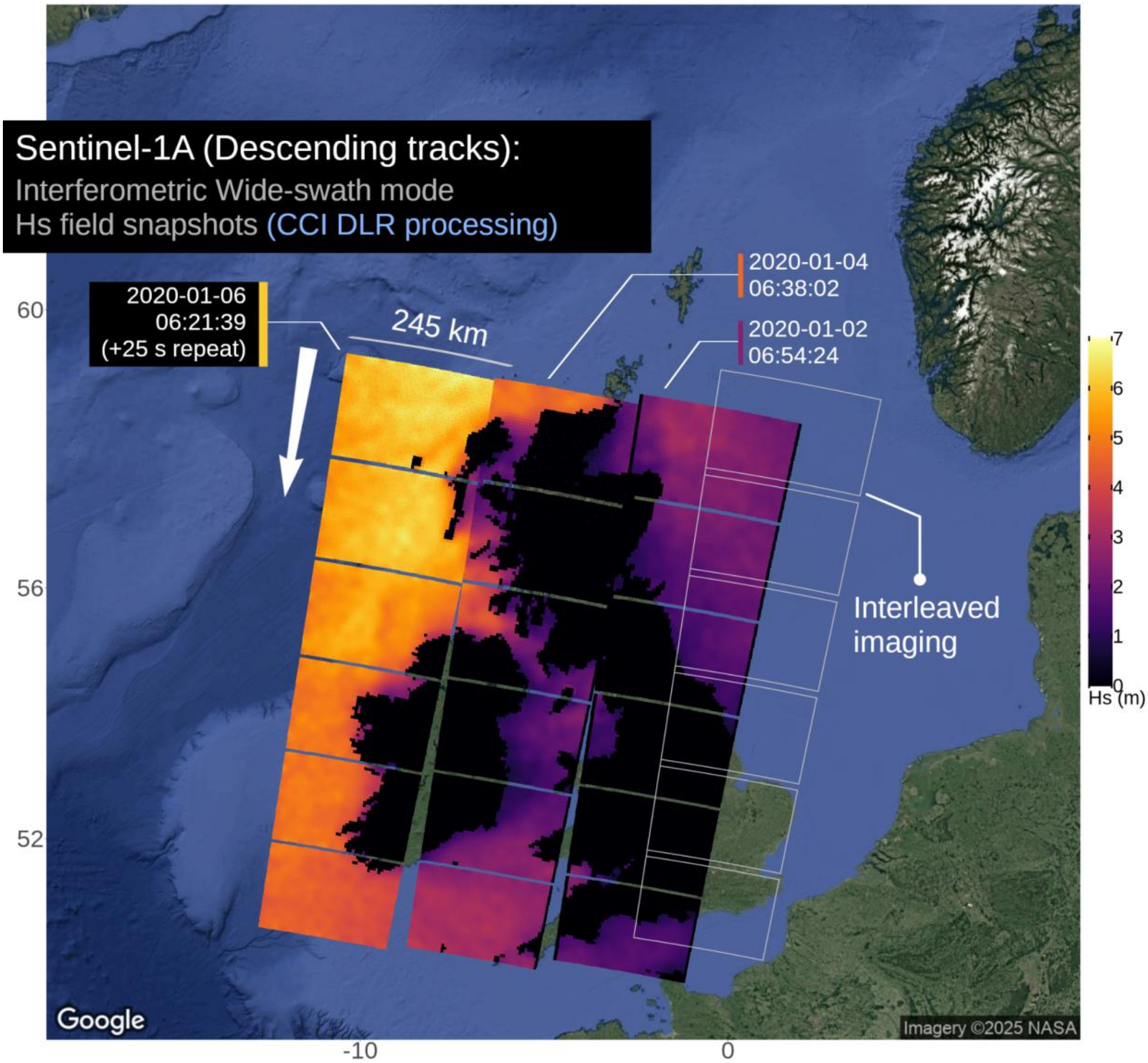

Figure 6.10: Hs fields from single imagettes from Sentinel-1A IW, captured in January 2020.

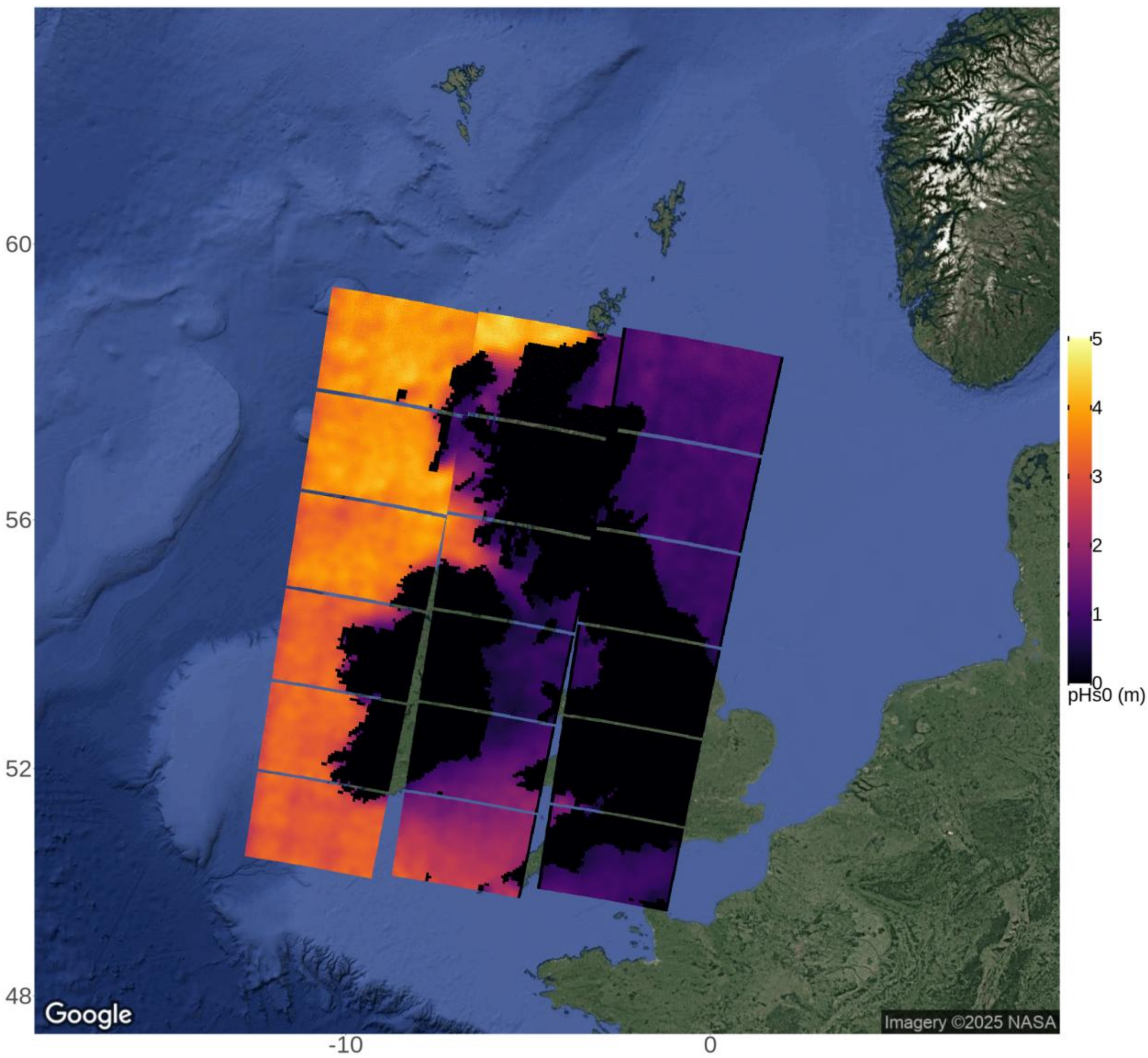

Figure 6.11: Swell primary Hs fields from single imagettes from Sentinel-1A IW, captured in January 2020.

Another example of S1A data is shown in Figure 6.12, where wave sheltering from the Caribbean Island of Anguilla is shown. Cells of data shown in black are associated with islands in the vicinity (quality flagged as “bad”). Although limited to spatial resolution of approximately 5 km, S1 IW data may prove valuable for applications in areas such as the Caribbean, including validation of local wave model output and regional conditions.

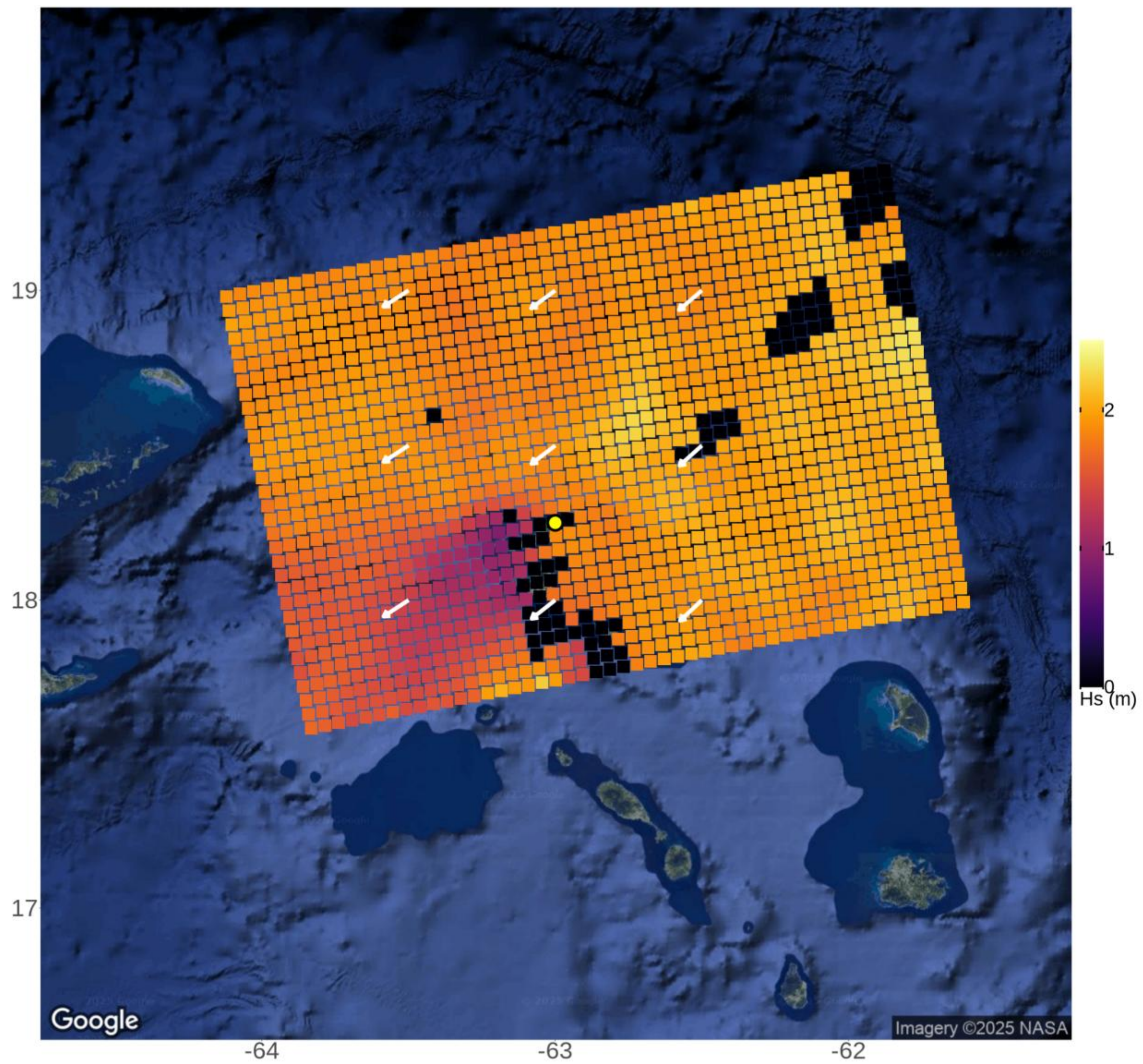

Figure 6.12: A Hs field from a single imagette from Sentinel-1A IW, captured in January 2017 around the Caribbean Island of Anguilla. For reference, wave direction from ERA5 monthly fields is denoted by white arrows.

6.4.2 Global summary

While S1 operates in IW mode over much of the global coastlines, it nonetheless captures a substantial amount of sea state data far from the shore. This is clear from a global analysis, where the European shelf is particularly heavily sampled. Sample counts on a 1° x 1° grid are shown in Figure 6.13. In this case, where a sufficiently large section of an individual IW mode imagette (> 100 points) intersects a particular grid cell, the median value is obtained, and counted as a single “super-observation”. This is somewhat analogous to taking an along-track average from altimeter data. Super-observations are then used to calculate statistics in the usual way.

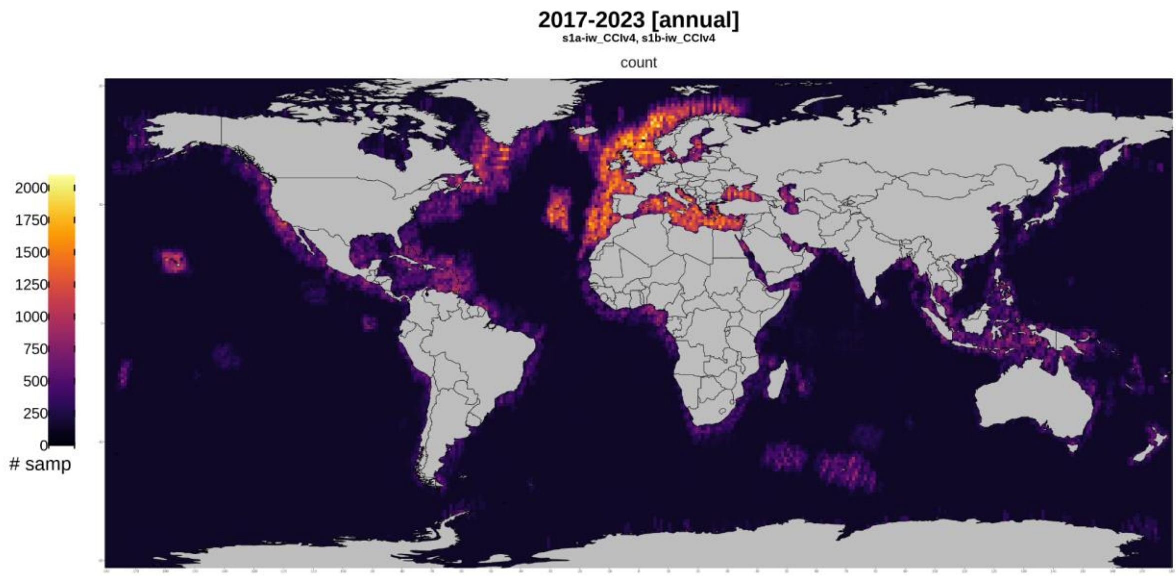

Figure 6.13: Total sample counts based on a 1° x 1° grid for Sentinel-1A/B IW mode during 2017 and 2023.

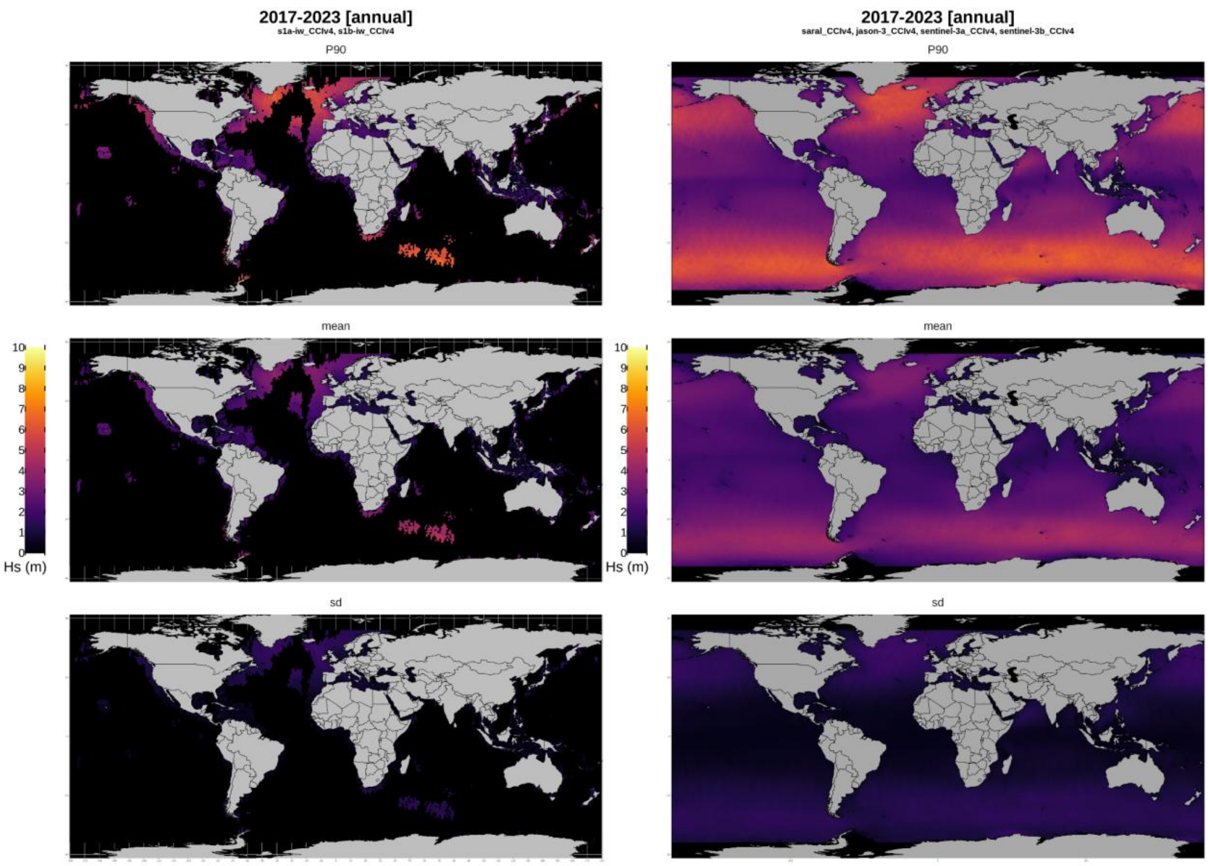

Figure 6.14: Hs statistics(annual) on a 1° x 1° grid for Sentinel-1A/B IW mode (left) during 2017 to 2023 and CCIv4 altimeters SARAL, Jason-3, Sentinel-3A/B (right).

Long term (2017-2023) wave statistics are shown in Figure 6.14 (left panels) compared with CCIv4 altimeters covering the same period. In this case, a sampling criteria of a minimum of

400 samples per grid cell is imposed in order to avoid spurious data. In fact, S1 IW mode captures small samples of data in many coastal and open ocean locations (removed here by the sampling criteria), but such data is insufficient to obtain meaningful long term statistics. Visually, agreement across the difference statistics appears to be reasonable but a global scale presentation is not particularly suitable for this type of data. A close up comparison over the North Atlantic, European shelf and Mediterranean is shown in Figure 6.15.

For the comparison of mean Hs we see fairly close agreement with CCIv4 altimetry at most offshore locations. However, there is a tendency for S1 IW to exceed the altimetry, which is particularly apparent in the eastern Atlantic, in the Bay of Biscay and at lower latitudes, where the discrepancy can reach ~20%. The Mediterranean shows spatial variability in agreement, although similar to elsewhere, S1 IW tends to be positive close to the coast.

In spite of limited sampling, Hs P90 statistics (Figure 6.15, top panel) from the two datasets show good agreement in many areas, seemingly better than the mean. Similar to the mean, coastal P90 appears to be consistently higher in the S1 data. Elsewhere, at least two regions of negative discrepancy (blue colour) are apparent. To the east of the U.K. and western Mediterranean S1 IW appears to be underestimating larger wave heights. Reasons for this are unclear although it is possible that sampling heterogeneity has led to selective undersampling (by S1) of more energetic sea states in these areas. These anomalies are also strongly apparent in the comparison of standard deviation (Figure 6.15, bottom panel). Negative differences in sd suggest that S1 IW is underestimating the variability, perhaps due to missing the extremes in these areas. Nonetheless, the cause of the regional distribution of these biases remains unknown. This will be investigated in future work.

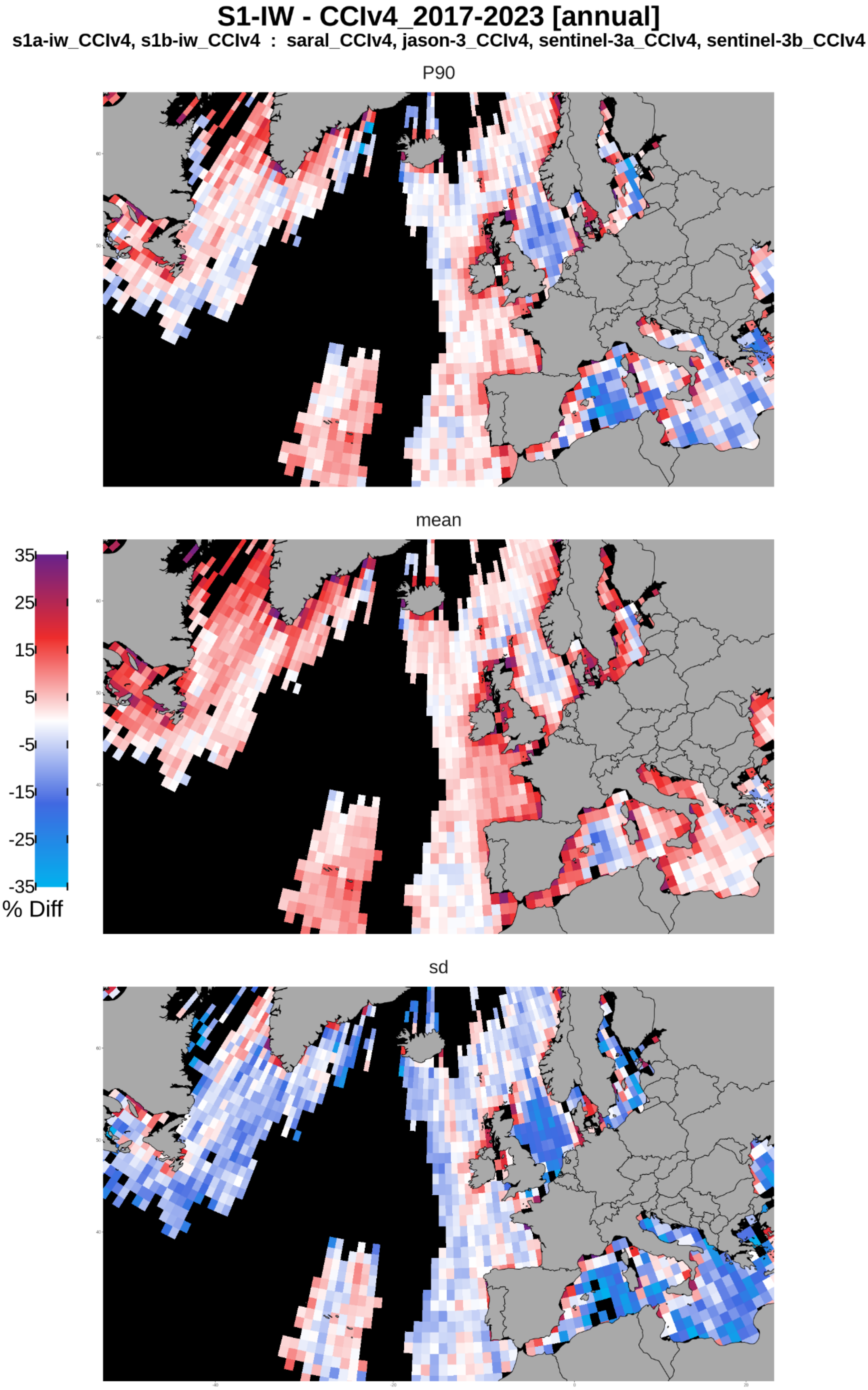

Figure 6.15: Differences in global annual climatological statistics of Hs between Sentinel-1A/B IW and CCIv4.

6.4.3 Coastal analysis

While the S1 IW mode CDR can be used to support larger scale regional applications (see e.g. Figure 6.15), it is rather better suited to smaller scale coastal studies, providing as it does, coverage of most global coastlines, with a limiting spatial resolution of ~5 km.

In this report, a short initial validation of S1 IW coastal sea state parameters is presented by comparing with the ResourceCode (RSCD) long term wave hindcast (see Section 2.3.1). High resolution coastal hindcasts like this dataset are particularly suitable since they provide a range of sea parameters that can be readily compared with the S1 observations, at a spatial resolution similar, or better than, S1 IW mode data.

The sea state parameters considered are total Hs, Tm2 and swell primary Hs.

6.4.3.1 Region of study

The RSCD domain spans the European shelf and Mediterranean, which provides substantial opportunity for intercomparison, in particular noting the coverage of S1 IW data. In this study, we select only a single image location captured over a region to the southwest of Ireland, shown in Figure 6.16 (see also Figure 6.10). For this site and image orientation (taken on the S1A descending pass), S1A has a revisit period of approximately two weeks. A long term study, based on S1A alone, therefore yields approximately 25 images per year, and close to 200 over the seven year period, 2017 to 2023, available in the CDR. In fact, data in this area could be substantially augmented through the use of S1A ascending tracks, and any spatially coincident data available from S1B (limited to 2017 to 2021).

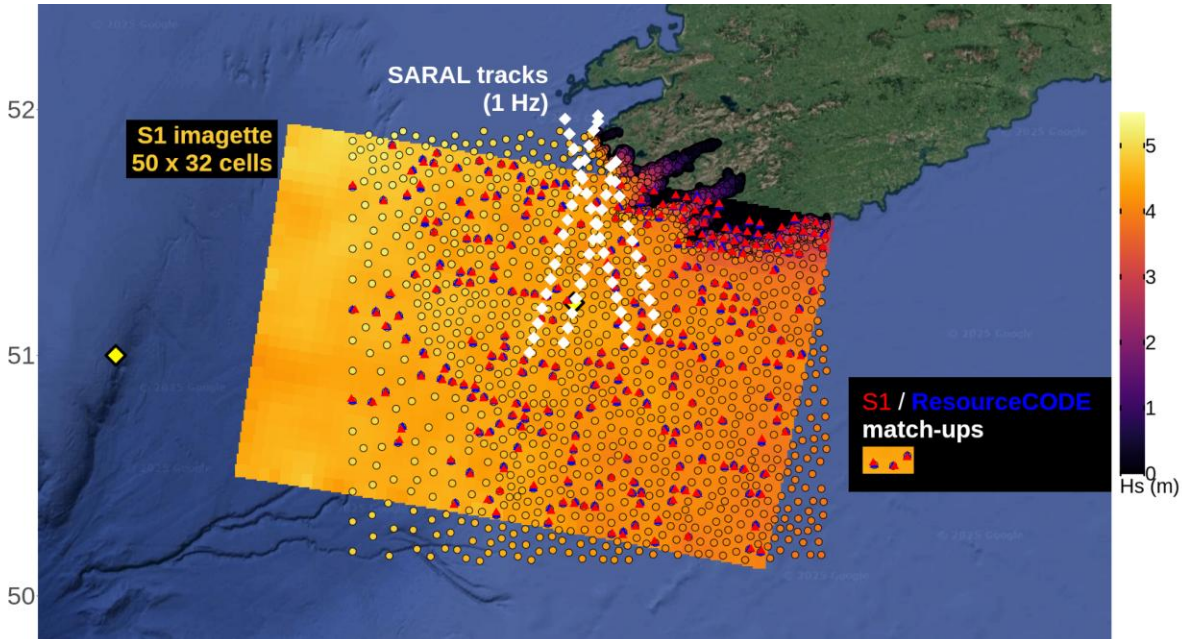

Figure 6.16: An example of Hs data from a descending pass of S1A is shown as the regular grid structure, comprising 50 x 32 cells, each approximately 5 x 5 km in spatial extent.

Corresponding data node locations from the RSCD hindcast unstructured grid are represented as circles. The fill colour indicates the model value of Hs. As an example of a possible collocation methodology, red and blue triangles indicate S1A cells and RSCD node points that are paired by using a maximum spatial separation criteria of ~1.5 km. Collocations form a random and heterogeneous distribution.
For reference, the locations of some coincident 1 Hz altimeter samples from SARAL are shown in white. Furthermore, the locations of two moored data buoys, operated by the U.K. MettOffice, are shown as yellow diamonds (one partially obscured by SARAL tracks).

Figure 6.16 shows an example of a possible collocation methodology between S1A and the RSCD data. Since the RSCD provides hourly data, temporal collocation with S1A (or other satellite) can be made within a 30 minute window. Together with an appropriate spatial collocation, a pairwise dataset can be created, from which detailed analysis can be conducted.

A possible spatial collocation scheme is illustrated in Figure 6.16. Hs data from an image from a descending pass of S1A is shown as a regular grid structure, comprising 50 x 32 cells, each approximately 5 x 5 km in spatial extent (see also Figure 6.10). Corresponding data node locations from the RSCD hindcast unstructured grid are represented as circles. The fill colour indicates the model value of Hs taken within 30 minutes of the S1A data. As an example of a collocation methodology, red and blue triangles respectively, indicate S1A cells and RSCD node points, that are paired by using a maximum spatial separation criteria of ~1.5 km. Collocations can be seen to form a random and heterogeneous distribution, although it turns out that many data locations do not meet this criteria. Nonetheless, a large number of collocations (~86,000) are identified for the S1A period of coverage (2017 to 2023).

Note that, for reference, in Figure 6.16 other relevant data sources are shown as examples and could be added to any analysis for further comparison. 1 Hz altimeter samples from SARAL are shown in white, and the locations of two moored data buoys, operated by the U.K. MettOffice, are shown as yellow diamonds (one partially obscured by SARAL tracks). Data from these sources is not considered in this example.

6.4.3.2 Analysis of parameters Hs, Tm2 and Swell primary Hs

Using the collocation methodology shown in Figure 6.16, the resulting pairwise dataset from S1A and RSCD produced the Hs anomaly statistics shown in Figure 6.17. For the entire annual data (Figure 6.17, panel A), agreement appears largely unbiased, although the data scatter is relatively high. RMSE w.r.t. A linear regression is found to be 0.47 m. A sea state dependent bias appears to lead to bias at higher values of Hs. For collocations conditioned on seasons (panels A-D), only small differences in the statistics can be seen. Nonetheless, the presence of some outlying data motivates further investigation.

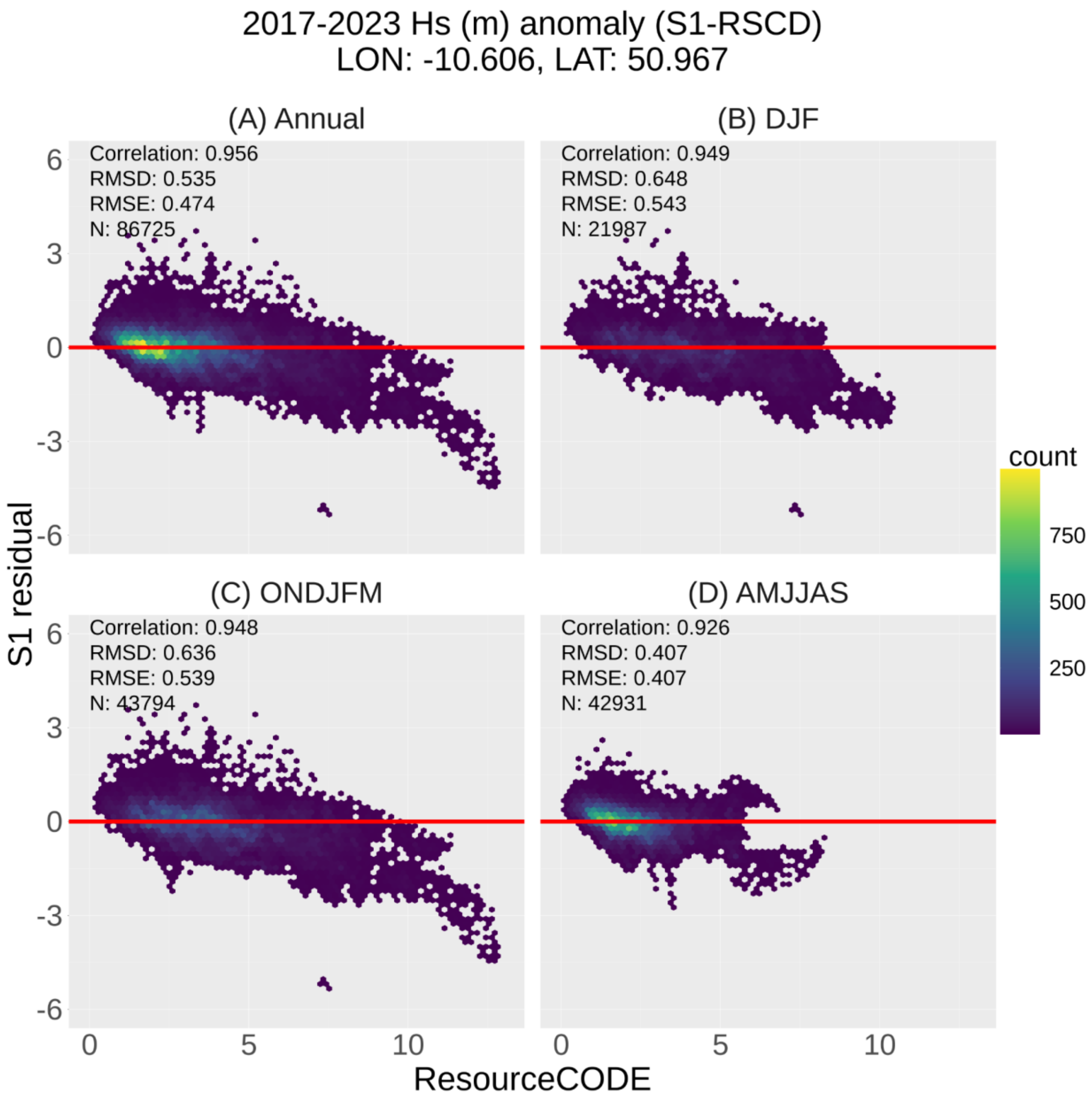

Figure 6.17: Hs anomaly from S1A and RSCD hindcast collocations (2017 to 2023) in the coastal and offshore waters to the southwest of Ireland (Fig. 6.16). Seasonal comparisons are shown in panels; Annual (A); DJF (B); ONDJFM (C); AMJJAS (D)

Anomaly statistics for Tm2, computed in the same way, are shown in Figure 6.18. In this case, correlation is typically still high (~0.9) but scatter is increased, with an RMSE from a linear regression found to be 0.61 s for the annual data (panel A). In the Atlantic, near Ireland, mean period Tm2 is typically lowest during the summer months (AMJJAS, panel D), which is when we see the poorest agreement between the two datasets. As seen for Hs, but more acute for Tm2, the presence of some scattered and widely outlying data motivates further investigation.

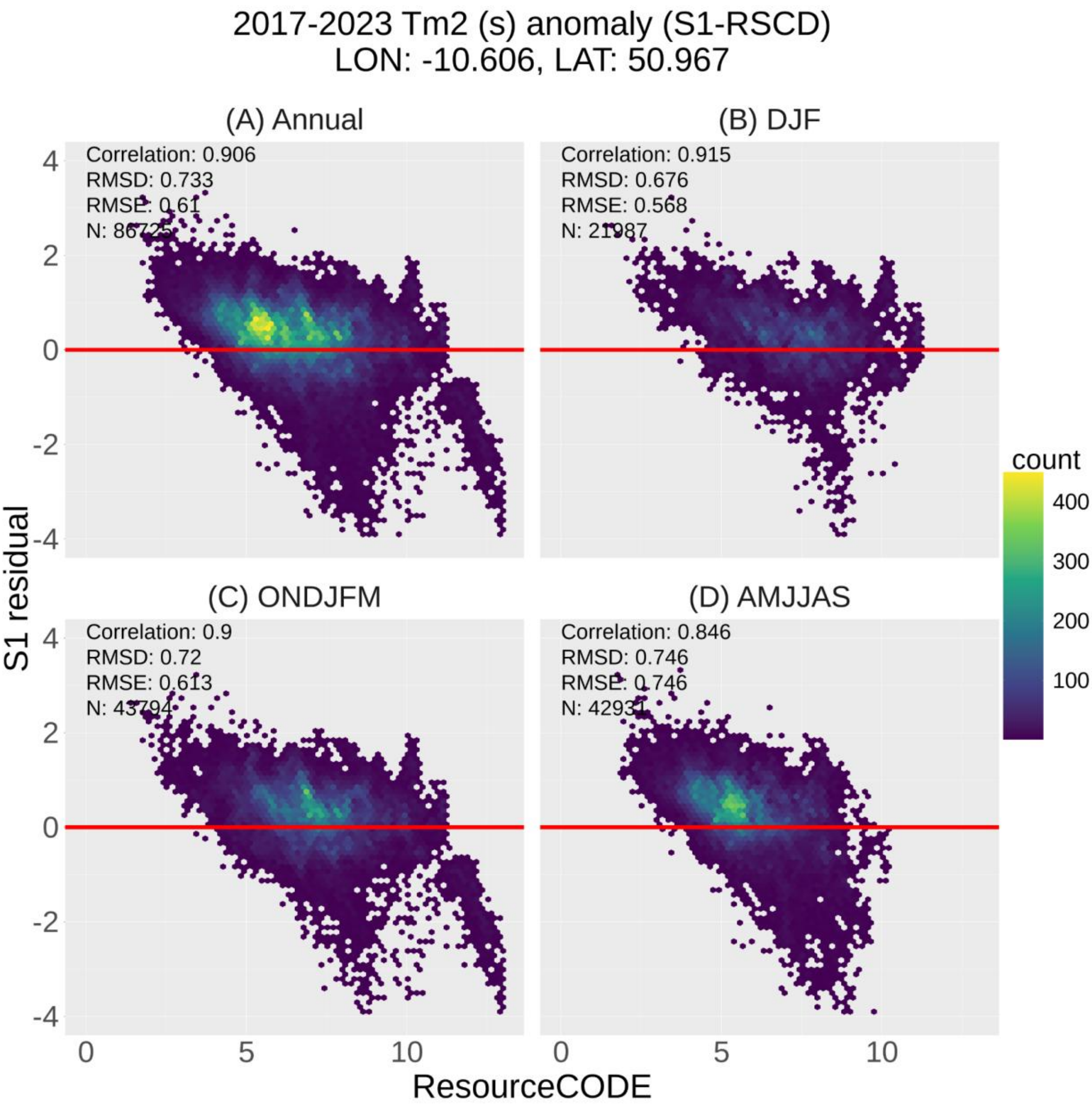

Figure 6.18: Tm2 anomaly from S1A and RSCD hindcast collocations (2017 to 2023) in the coastal and offshore waters to the southwest of Ireland (Fig. 6.16). Seasonal comparisons are shown in panels; Annual (A); DJF (B); ONDJFM (C); AMJJAS (D)

The final parameter to consider in this section is swell primary Hs. Anomaly statistics are shown in Figure 6.19. In this case, agreement between the two datasets is poorest, with correlation ranging between 0.57 and 0.71. Most apparent is a strong Hs dependent bias in S1A where estimates are low w.r.t. to RSCD. This bias does not appear to be substantially affected by season. Since accurate ocean swells can be difficult to model numerically (see e.g. PVP section 3), particularly their timing, it is possible that these strong biases are due to temporal misalignment, and that the model data may be at fault. However, a more detailed investigation is required, and these results suggest that swell Hs data should be used with caution.

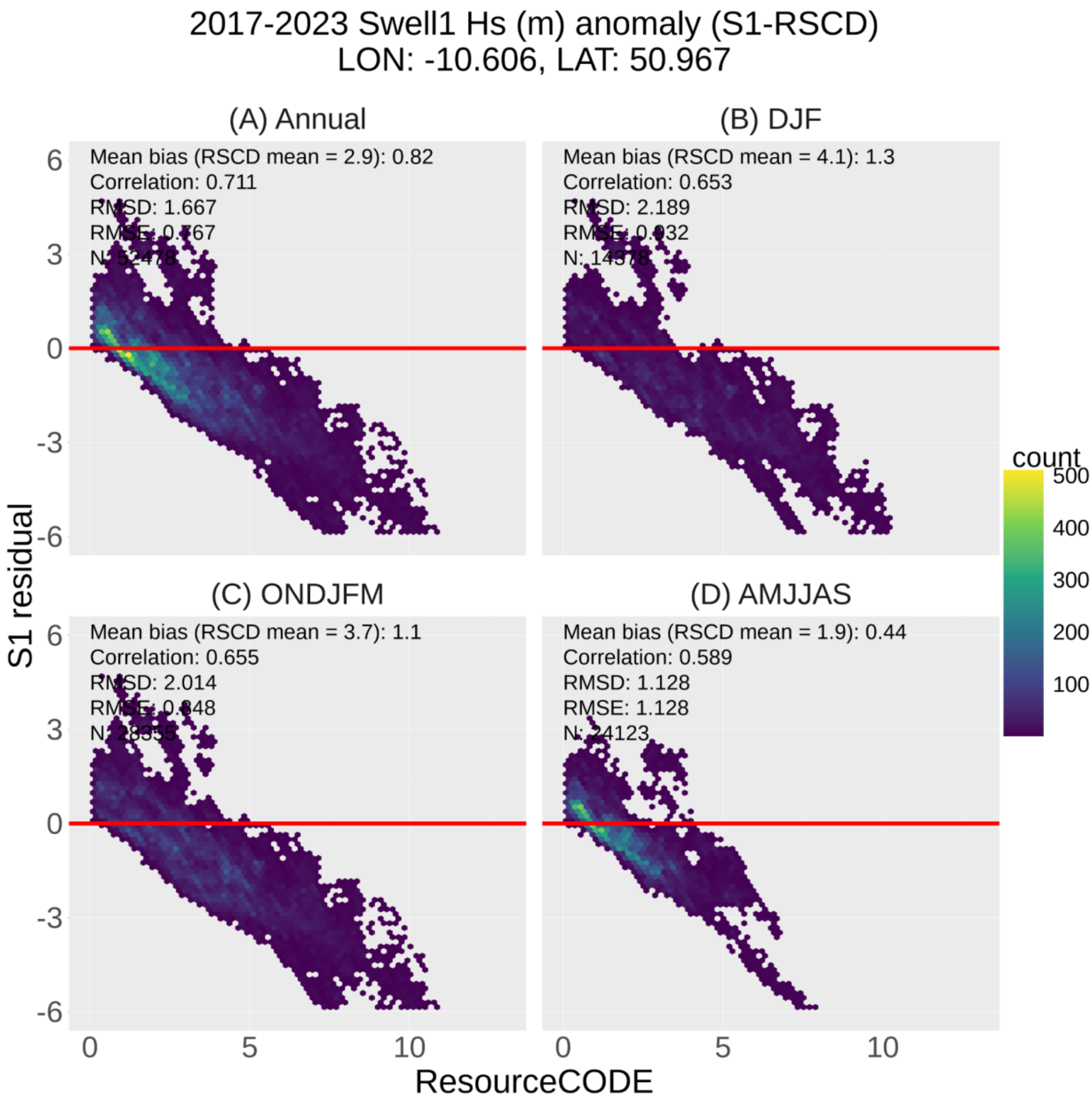

Figure 6.19: Swell primary Hs anomaly from S1A and RSCD hindcast collocations (2017 to 2023) in the coastal and offshore waters to the southwest of Ireland (Fig. 6.16). Seasonal comparisons are shown in panels; Annual (A); DJF (B); ONDJFM (C); AMJJAS (D)

6.4.3.3 Spatial analysis of Hs

Intercomparisons in the previous section, based upon aggregate collocation of S1A and RSCD data within an S1A image domain, provide useful insights, but have the disadvantage of losing the detailed spatial information provided by the S1 IW mode CDR. Indeed, a particular novelty and benefit of the S1 IW mode data is that spatial variation of sea state, including long term sea state gradients, may be obtained within the image domain (e.g. Figure 6.16). Such information can also be found from altimetry data, where altimeters frequently revisit on the same orbit, but this is limited to only the along-track direction. In this respect, S1 offers considerably more information with complete direction coverage. Using the same spatial domain, an example of results from a spatial comparison with RSCD, is shown in Figures 6.20 and 6.21.

In this case, a new longitude / latitude grid is defined within the collocation domain, with a bin size of approximately 15 km square. The collocation criteria is now modified to include all data available within those bins. We consider only mean Hs climatology (2017 to 2023) from S1A for the domain, which is shown in Figure 6.20. The magnitude of the mean, strongly dependent on seasons, ONDJFM and AMJJAS, is shown in panels A and B respectively. Within the new grid, data seem spatially coherent and the gradients seem reasonable, although in Figure 6.20(A), lower values of Hs can be seen to the north, where one might expect more consistency with data further south, due to exposure to the North Atlantic.

Using a similar binning methodology for the RSCD data, the mean Hs from the two datasets can be compared on the same spatial grid. Results are shown in Figure 6.21. As seen in Figure 6.17, for most of the collocation domain, RSCD has a tendency for higher values of Hs, apparently increasing with increasing distance to coast up to around 0.3 m offshore. However, agreement is better at lower values of Hs, typically seen during the summer. These fairly small discrepancies in the mean suggest good data consistency and are encouraging. Extremely negative differences (strong blue colours), seen close to the coast, are very likely related to inappropriate spatial match-ups associated with a strong conflict of spatial resolutions very close to the coast RSCD providing data at separations of ~300 m, compared with 5 km from S1A).

Finally, we note that although bias may be present, in one or other of the datasets, gradient information is available from S1A and shown clearly in Figures 6.20 and 6.21. However, a peculiar zonal band is apparent in the most northerly data. This remains unexplained but is very likely related to data sampling heterogeneity, rather than real discrepancy in the data. Data collocation on misaligned grids, as is the case here (See Figure 6.16), can introduce sampling issues if not carefully implemented. This remains a matter for further investigation. Analysis over a wider domain is desirable but beyond the scope of this report. Additionally, the spatial collocation grid employed here, with ~15 km bins, could be further refined, since S1A provides data at a scale of ~5 km.

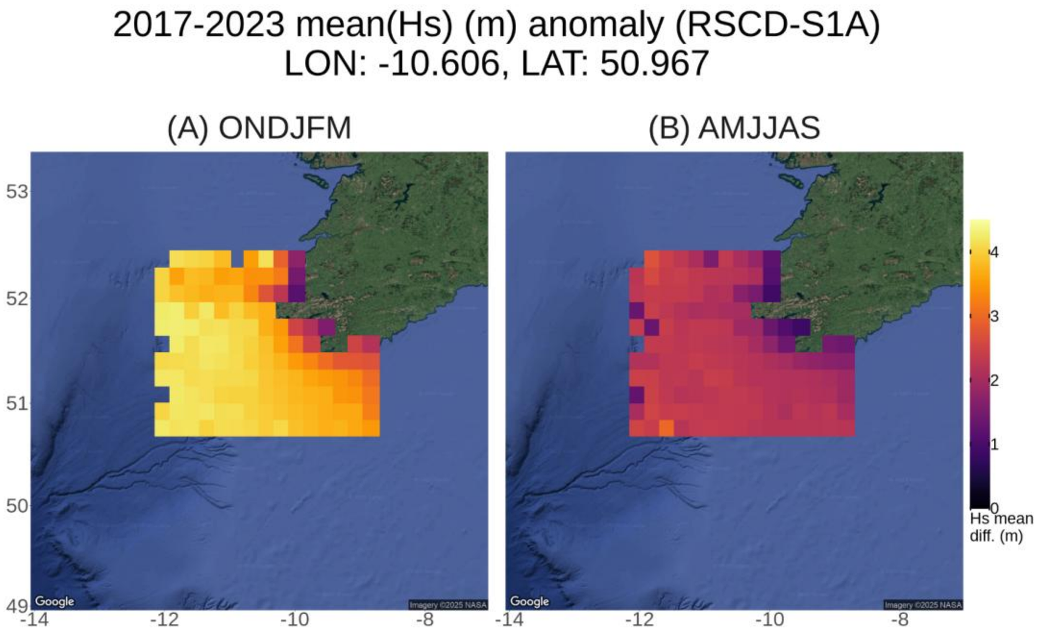

Figure 6.20: Mean Hs from S1A (2017 to 2023) in the coastal and offshore waters to the southwest of Ireland. Seasonal comparisons are shown; ONDJFM (A); AMJJAS (B)

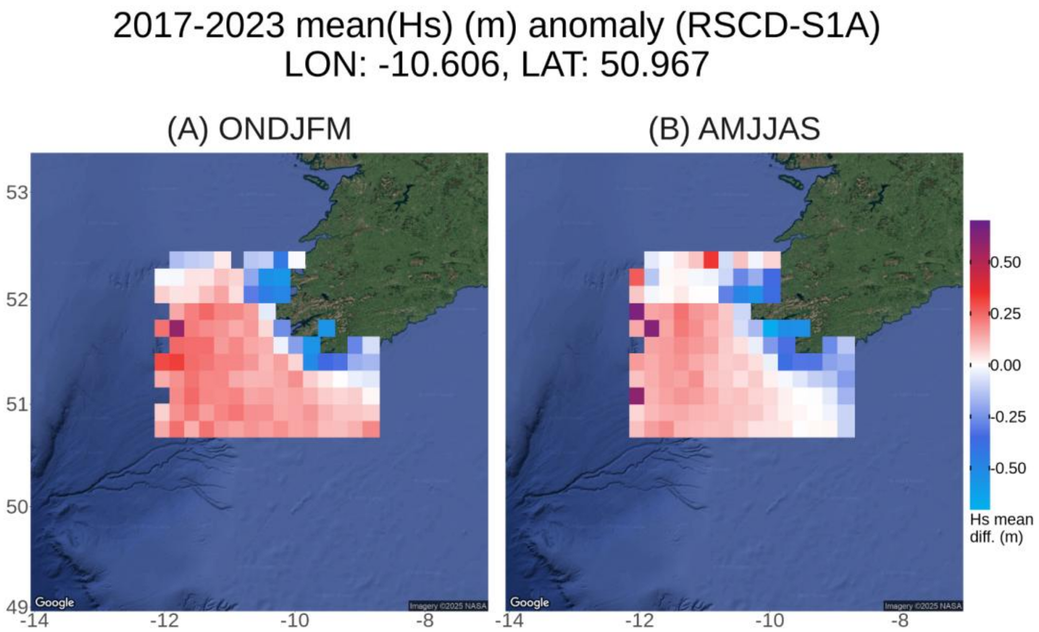

Figure 6.21: Mean Hs from S1A (2017 to 2023) in the coastal and offshore waters to the southwest of Ireland. Seasonal comparisons are shown; ONDJFM (A); AMJJAS (B)

7. Conclusions and Future work

This report captures results from the validation and intercomparison of the Sea State CCI version 4 CDRs with a variety of high quality reference data. In general, while areas of discrepancy have been identified across all CDRs and reference data, very few dramatic data conflicts have been identified. Nonetheless, the abundance of new data within the version 4 CDRs, in particular the range of new parameters from Sentinel-1 SAR modes, both offshore and coastal, motivate further and on-going studies. Within the limits of available resources, updates to this document will be provided with the release of version 5 CDRs, anticipated in early 2026.

7.1 Key Findings

Overall, in most cases the version 4 CDRs have been found to compare closely with high quality reference sea state datasets. Key points are identified as follows:

- Hs trends (Sections 3 and 4): Addition of the newly intercalibrated ERS-1/2 and Topex altimetry data extends the version 3 CCI altimetry Level-2 along-track and Level-4 gridded CDRs back in time to 1992. However, in terms of seasonal climatological values of Hs over the record, these missions show a divergence (up to 10% in mean Hs) from other widely used datasets such as RY2023 and ERA5. This has the effect of increasing Hs long term trend estimates compared to the earlier version 1 CDR, although note that updated global trends over the extended time period (up to 2023), calculated following the approach of the PVIR version 3 (phase 1), appear to show lower gradient magnitudes overall. Furthermore, over the past 20 years only, very strong agreement was found in mean Hs trends between the CCI Level-4 and ERA5 data.
- Low sea states (Section 5): A range of discrepancies, mostly associated with the low climatological wave heights of the sub-tropical and swell dominated regions, have been identified between CCI CDRs and other reference data sources. These affect both evaluations from altimetry and SAR data. Such discrepancies have been identified previously (see e.g. PVIR version 2), but persist without a detailed explanation.
- Section 6.2.3: The Ifremer processing of Hs from Sentinel-1A/B WV mode shows a discrepancy with respect to both the DLR processing of the same mission, and the version 4 CCI altimetry CDRs. In particular, larger wave heights associated with long term P90 Hs (> ~5 m) appear to be underestimated by at least 20% in some areas. The causes of this discrepancy are not yet understood and so caution is advised. Note also that no intercalibration between altimetry and SAR datasets has yet been undertaken.
- A preliminary analysis of mean wave period (Tm2) and swell1 Hs partition data from the DLR S1A/B WV CDR, shows generally good agreement with ERA5 mean fields over much of the globe. As noted elsewhere, some strong disagreements have been seen regionally, usually associated with sub-tropical and swell dominated regions.
- Polar regions have not been considered explicitly and marginal ice zones are likely to be contaminated, so analysis within these areas should be undertaken with caution.
- A range of data from different operating modes of Sentinel-1, is provided in CCI version 4 CDRs, although at this time, no independent validation of this data has yet been undertaken. These data include; Hs windsea, swell secondary Hs, further period

parameters beyond Tm2, and the entire processing of "Extra-wide Swath Mode" (EW). Users are advised to proceed with caution.

7.2 Future Updates

Key areas for updates in the next revision of this document are identified as follows:

- It is intended that Sentinel-1A/B IW mode data will be expanded to further geographic regions through the use of other high resolution regional hindcasts.
- Time series of wave parameters from a limited number of moored buoys will be examined (see e.g. PVIR version 2).
- Hourly ERA5 data will be processed to provide more extreme measure of Hs, beyond the limitations of monthly fields.
- Additional long term wave data from (non-assimilating) hindcasts will be used to augment climatological and trend analysis.

8. References

Aarnes et al. (2015) Marine Wind and Wave Height Trends at Different ERA-Interim Forecast Ranges *J. Clim.* https://doi.org/10.1175/JCLI-D-14-00470.1

Ablain, Michaël et al. (2019) Uncertainty in satellite estimates of global mean sea-level changes, trend and acceleration. *Earth Syst. Sci. Data, 11, 1189–1202* https://doi.org/10.5194/essd-11-1189-2019

Accensi, M., Alday, M., Maisondieu, C., Raillard, N., Darbynian, D., Old, C., Sellar, B., Thilleul, O., Pérignon, Y., Payne, G., O'Boyle, L., Fernandez, L., Dias, F., Chumbinho, R. & Guitton, G. (2021). Resourcecode framework: A high-resolution wave parameter dataset for the European shelf and analysis toolbox*, Proceedings of the European Wave and Tidal Energy Conference: 14th EWTEC 5-9th September 2021 Plymouth, UK EWTEC, https://proceedings.ewtec.org/product/ewtec-2021-plymouth-uk/*

Alday, M. & Ardhuin, F. (2023). On consistent parameterizations for both dominant wind-waves and spectral tail directionality. *Journal of Geophysical Research: Oceans, 128,* https://doi.org/10.1029/2022JC019581

Ardhuin, F., R. Magne, J-F. Filipot, A. Van der Westhyusen, A. Roland, P. Quefeulou, J. M. Lefèvre, L. Aouf, A. Babanin and F. Collard (2010) Semi empirical dissipation source functions for wind-wave models : Part I, definition and calibration and validation at global scales. *Journal of Physical Oceanography*.

Ardhuin, F., Stopa, J. E., Chapron, B., Collard, F., Husson, R., Jensen, R. E., et al. (2019). Observing sea states. *Frontiers, 6, 124.* https://doi.org/10.3389/fmars.2019.00124

Casas-Prat, M., Mark A. Hemer, Guillaume Dodet, Joao Morim, Xiaolan L. Wang, Nobuhito Mori, Ian Young, Li Erikson, Bahareh Kamranzad, Prashant Kumar, Melisa Menéndez & Yang Feng (2024) Wind-wave climate changes and their impacts *Nature Reviews Earth & Environment volume 5, pages 23–42* https://doi.org/10.1038/s43017-024-00518-0

CMEMS. accessed 2024. Copernicus Marine Environment Monitoring Service. https://marine.copernicus.eu/

Collard, F., F. Ardhuin, and B. Chapron (2009), Monitoring and analysis of ocean swell fields from space: New methods for routine observations, *J. Geophys. Res., 114, C07023,* https://doi.org/10.1029/2008JC005215

De Carlo, M., Ardhuin, F., Ollivier, A., & Nigou, A. (2023). Wave groups and small scale variability of wave heights observed by altimeters. *Journal of Geophysical Research: Oceans, 128.* https://doi.org/10.1029/2023JC019740

De Carlo, M., Ardhuin, F. (2024). Along-track resolution and uncertainty of altimeter-derived wave height and sea level: re-defining the significant wave height in extreme storms . *Journal of Geophysical Research: Oceans,* Dodet, G. et al. (2020) The Sea State CCI dataset v1: Towards a Sea State Climate Data Record based on satellite observations. *Earth Syst. Sci. Data* http://dx.doi.org/10.5194/essd-12-1929-2020

Dodet, G.; Abdalla, S.; Alday, M.; Accensi, M.; Bidlot, J.; Ardhuin, F. Error Characterization of Significant Wave Heights in Multidecadal Satellite Altimeter Product, Model Hindcast and In Situ Measurements Using the Triple Collocation Technique. *Journal of Atmospheric and Oceanic Technology, 39, 887–901.* https://doi.org/10.1175/JTECH-D-21-0179.1

Donlon et al. (2021) Enhanced continuity of satellite sea level measurements from space. *Remote Sensing of Environment* https://doi.org/10.1016/j.rse.2021.112395

Gemmrich, J., Thomas, B., & Bouchard, R. (2011). Observational changes and trends in northeast Pacific wave records. *Geophysical Research Letters, 38, L22601.* https://doi.org/10.1029/2011GL049518

Girard-Ardhuin, F., Ezraty, R., 2012. Enhanced Arctic Sea Ice Drift Estimation Merging Radiometer and Scatterometer Data. *IEEE Transactions on Geoscience and Remote Sensing 50, 2639–2648* https://doi.org/10.1109/TGRS.2012.2184124

Gourrion, J., D. Vandemark, S. Bailey, B. Chapron, G. P. Gommenginger, P. G. Challenor, and M. A. Srokosz, (2002): A Two-Parameter Wind Speed Algorithm for Ku-Band Altimeters. J. Atmos. Oceanic Technol., 19, 2030–2048, https://doi.org/10.1175/1520-0426(2002)019<2030:ATPWSA>2.0.CO;2

Graham, J. A. et al. (2018) AMM15: a new high-resolution NEMO configuration for operational simulation of the European north-west shelf. *Geosci. Model Dev., 11, 681–696.* https://doi.org/10.5194/gmd-11-681-2018

Hall, C. & Jensen, R.E. (2022) USACE Coastal and Hydraulics Laboratory Quality Controlled, Consistent Measurement Archive. *Scientific Data, 9.* https://doi.org/10.1038/s41597-022-01344-z

Hauser et al. (2021) New observations from the swim radar on-board CFOSat: Instrument validation and ocean wave measurement assessment. *IEEE Trans. Geosci. Rem. Sens., Vol. 59, No. 1.* https://doi.org/10.1109/TGRS.2020.2994372

Hersbach, H. et al. (2020) The ERA5 global reanalysis. *Q. J. R. Meteorol. Soc. 146 (730), 1999–2049.* http://dx.doi.org/10.1002/qj.3803

Hirsch, R.M.; Slack, J.R.; Smith, R.A. Techniques of trend analysis for monthly water quality data. *Water Resour. Res. 1982, 18, 107–121.*

Hochet, A., Dodet, G., Sévellec, F., Bouin, M.-N., Patra, A., & Ardhuin, F. (2023). Time of emergence for altimetry-based significant wave height changes in the North Atlantic. *Geophysical Research Letters, 50,* https://doi.org/10.1029/2022GL102348c

Houghton, A. I, et al. (2021) Performance Statistics of a Real-Time Pacific Ocean Weather Sensor Network. *J. Atmos. Oc. Tech. 1047-1058, 58* https://doi.org/10.1175/JTECH-D-20-0187.1

Janssen, P., L. Aouf, A. Behrens, G. Korres, L. Cavalieri, K. Christiensen, O. Breivik : Final report of work-package I in my wave project. December 2014.

Jiang, H. (2020) Evaluation of altimeter undersampling in estimating global wind and wave climate using virtual observation. *Remote Sensing of Environment, 245, 111840* https://doi.org/10.1016/j.rse.2020.111840

Jiang et al. (2022) Validation of Wave Spectral Partitions From SWIM Instrument On-Board CFOSAT Against In Situ Data. *IEEE Trans. Geosci. Rem. Sens. Vol. 60* https://doi.org/10.1109/TGRS.2021.3110952

Jiang, H. Random, Environmental, and Representativeness Errors in Ocean Remote Sensing Versus In Situ Data: An Example of Wave Heights From Altimeters. *IEEE Transactions on Geoscience and Remote Sensing*. https://doi.org/10.1109/TGRS.2023.3285348

Liu et al. (2021) Global Wave Hindcasts Using the Observation-Based Source Terms: Description and Validation https://doi.org/10.1029/2021MS002493

Liu et al. (2023) On global wave height climatology and trends from multiplatform altimeter measurements and wave hindcast, *Ocean Modelling, 186 102264,* https://doi.org/10.1016/j.ocemod.2023.102264

Livermont, E., 2017. Correcting changes in the NDBC wave records of the United States. 15th International Workshop on Wave Hindcasting and Forecasting, Liverpool, UK, September 10-15.

Mason, T.; Dhoop, T. Quality Assurance & Quality Control of Wave Data. Available online: http://www.channelcoast.org/ccoresources/dataqualitycontrol (accessed on 2024-04-09)

Mcallister & van den Bremer (2019) Lagrangian Measurement of Steep Directionally Spread Ocean Waves: Second-Order Motion of a Wave-Following Measurement Buoy JPO https://doi.org/10.1175/JPO-D-19-0228.1

Meucci et al. (2020) Comparison of Wind Speed and Wave Height Trends from Twentieth-Century Models and Satellite Altimeters, *J. Clim, Vol. 33, 611-624.* https://doi.org/10.1175/JCLI-D-19-0540.1

Morim et al. (2019) Robustness and uncertainties in global multivariate wind-wave climate projections, *Nature Climate Change, Vol. 9, 711-718.* https://doi.org/10.1038/s41558-019-0542-5

Nencioli, F. and Quartly, G.D. (2019) Evaluation of Sentinel-3A Wave Height Observations Near the Coast of Southwest England. *Remote Sensing, 11.* https://doi.org/10.3390/rs11242998

Pleskachevsky, A., B. Tings, S. Jacobsen, “Multiparametric Sea State Fields from Synthetic Aperture Radar for Maritime Situational Awareness”, *RSE, 2022, vol. 280,* https://doi.org/10.1016/j.rse.2022.113200

Pleskachevsky, A., B. Tings, S. Jacobsen, S. Wiehle, E. Schwarz, D. Krause, “A System for Near Real Time Monitoring of the Sea State using SAR Satellites”, *TGRS,* 2024 https://doi.org/10.1080/01431161.2018.1558377

Quach, B., Yannik Glaser, Justin Stopa, Alexis Mouche and Peter Sadowski. Deep Learning for Predicting Significant Wave Height From Synthetic Aperture Radar. *IEEE Transactions on Geoscience and Remote Sensing, 2021, 59 (3), pp.1859-1867* https://doi.org/10.1109/TGRS.2020.3003839

Quilfen, Y. & Chapron, B. (2019) Ocean surface wave-current signatures from satellite altimeter measurements. *Geophysical Research Letters, 46, 253–261.* https://doi.org/10.1029/2018GL081029

Quilfen, Y. & Chapron, B., (2020) On denoising satellite altimeter measurements for high-resolution geophysical signal analysis. *Advances in Space Research.* https://doi.org/10.1016/j.asr.2020.01.005

Ribal, A. and Young, I.R. 33 years of globally calibrated wave height and wind speed data based on altimeter observations. *Sci. Data 2019, 6, 1–15.* http://dx.doi.org/10.1038/s41597-019-0083-9

Timmermans, B. et al. (2020a) Global Wave Height Trends and Variability from New Multimission Satellite Altimeter Products, Reanalyses, and Wave Buoys. *Geophys. Res. Lett. 2020, 47, 1–11* https://doi.org/10.1029/2019GL086880

Timmermans, B. et al. (2020b) Reliability of Extreme Significant Wave Height Estimation from Satellite Altimetry and In Situ Measurements in the Coastal Zone, *J. Mar. Sci. Eng. 2020, 8, 1039* https://doi.org/10.3390/jmse8121039

Timmermans et al. (2022) Product Validation and Intercomparison Report, version 2

Timmermans et al. (2024) Uncertainties in sea state observations from satellite altimeters and buoys during the Jason-3/Sentinel-6 MF Tandem Experiment. *Remote Sensing*

Wang, H. et al. (2022a) Determining Errors in Directional Buoy-Derived Swell Heights via the Joint Analysis of Space-Borne Radars and WaveWatch III Simulations. *IEEE Geo. Rem. Sens. Let., Vol. 19*

Wang H. et al. (2022b) Quantifying Uncertainties in the Partitioned Swell Heights Observed From CFOSAT SWIM and Sentinel-1 SAR via Triple Collocation. *IEEE Trans. Geo. Rem. Sens, Vol. 60* https://doi.org/10.1109/TGRS.2022.3179511

Yang, Z., Gabriel García Medina, Vincent S. Neary, Seongho Ahn, Levi Kilcher, Aidan Bharath (2023) Multi-decade high-resolution regional hindcasts for wave energy resource characterization in U.S. coastal waters. Renewable Energy Volume 212, August 2023, 803-817 https://doi.org/10.1016/j.renene.2023.03.100

Young, I. R. (1986) Probability Distribution of Spectral Integrals, *Journal of Waterway, Port, Coastal, and Ocean Engineering Vol. 112, No. 2* https://doi.org/10.1061/(ASCE)0733-950X(1986)112:2(338)

Young, I. R. & Ribal, A. (2019). Multiplatform evaluation of global trends in wind speed and wave height. *Science, 364, 548–552.* https://doi.org/10.1126/science.aav9527

Young, I.R. & Ribal, A. (2022) Can Multi-Mission Altimeter Datasets Accurately Measure Long-Term Trends in Wave Height? *Remote Sens. 14, 974.* https://doi.org/10.3390/rs14040974